Explicitly Simulated Electrification and Lightning within a Tropical Cyclone Based on the Environment of Hurricane Isaac (2012)

ALEXANDRE O. FIERRO

Cooperative Institute for Mesoscale Meteorological Studies, University of Oklahoma, and NOAA/OAR/National Severe Storms Laboratory, Norman, Oklahoma

EDWARD R. MANSELL, CONRAD L. ZIEGLER, AND DONALD R. MACGORMAN

NOAA/OAR/National Severe Storms Laboratory, Norman, Oklahoma

(Manuscript received 15 December 2014, in final form 8 May 2015)

ABSTRACT

This work analyzes a high-resolution 350-m simulation of the electrification processes within a hurricane in conjunction with available total lightning observations to augment the general understanding of some of the key cloud-scale electrification processes within these systems. The general environment and trends of Hurricane Isaac (2012), whose lightning activity was observed by the Earth Networks Total Lightning Network, were utilized to produce a reasonable tropical cyclone simulation. The numerical model in this work employs explicit electrification and lightning parameterizations within the Weather Research and Forecasting Model.

Overall, simulated storm-total flash origin density rates remain comparable to the observations. Because simulated reflectivities were larger and echo tops were higher in the eyewall than observed, the model consistently overestimated lightning rates there. The gross vertical charge structure in the eyewall resembled a normal tripole or a positive dipole, depending on the location. The negative charge at middle levels and positive at upper levels arose primarily from noninductive charging between graupel and ice crystals/snow. As some graupel melted into rain, the main midlevel negative charge region extended down to the surface in some places. The large volume of positively charged snow aloft caused a radially extensive negative screening layer to form on the lighter ice crystals above it.

Akin to continental storms and tropical convection, lightning activity in the eyewall was well correlated with the ice water path ($r > 0.7$) followed by the graupel + hail path ($r \approx 0.7$) and composite reflectivity at temperatures less than -10°C and the snow + ice path ($r \approx 0.5$). Relative maxima in updraft volume, graupel volume, and total lightning rates in the eyewall all were coincident with the end of an intensification phase.

1. Introduction

Landfalling tropical cyclones (TCs) pose considerable threat to coastal communities and present one of the major challenges for operational forecasters, particularly those TCs undergoing rapid intensification or ''RI'' (Kaplan and DeMaria 2003; Kaplan et al. 2010). In recent years, significant progress has been made toward forecasting the tracks of TCs (e.g., Marks and Shay 1998). This is because TC tracks largely are governed by the synoptic-scale steering flow, which current operational models have been able to resolve with a reasonable degree of realism, especially in the last decade (Hendricks et al. 2011). In comparison, however, less progress has been made toward forecasting TC intensity (DeMaria et al. 2014). This is because intensity fluctuations within TCs primarily are controlled by small-scale, transient, hard-to-forecast, moist convective processes in the TC inner core or eyewall. Because the convection embedded within the eyewall of a TC evolves in a vorticity-rich environment, some of these small-scale convective events are known as ''vortical hot towers'' (VHTs; Hendricks et al. 2004; Montgomery et al. 2006).

The VHTs, which are characterized by locally large moist static energy and relative vertical vorticity, may become axisymmetrized around the inner core by the horizontal shear of the tangential wind during

Corresponding author address: Alexandre O. Fierro, CIMMS, National Weather Center, Suite 2100, 120 David L. Boren Blvd., Norman, OK 73072.
E-mail: alex.fierro@noaa.gov

DOI: 10.1175/JAS-D-14-0374.1

intensification (e.g., Anthes 2003; Nolan et al. 2007; Guimond et al. 2010). In particular, recent observational and modeling studies have suggested that the locally enhanced latent heating produced by condensation and freezing within hot towers embedded in the eyewall is often accompanied by the intensification or even by the rapid intensification of the TC (e.g., Nolan et al. 2007; Guimond et al. 2010). Because of the strong tie between convection and lightning, it is anticipated that relationships exist between eyewall lightning activity and TC intensity.

The appearance of graupel or small hail aloft, and the associated increase in reflectivity, is indicative of strong updrafts and an increased probability for lightning flashes to occur (MacGorman et al. 1989; MacGorman and Rust 1998). Consistent with this, numerous observational studies spanning most TC-prone oceanic basins worldwide stressed the importance of a more systematic monitoring of changes in TC lightning flash activity (Lyons et al. 1989; Molinari et al. 1994, 1999; Orville and Coyne 1999; Cecil and Zipser 2002; Kelley et al. 2004; Samsury and Orville 1994; Shao et al. 2005; Squires and Businger 2008; Price et al. 2009; Thomas et al. 2010; Fierro et al. 2011; Fierro and Reisner 2011; DeMaria et al. 2012; Bovalo et al. 2014; Stevenson et al. 2014; Pan et al. 2010, 2014) as such activity is recognized as a very useful indicator of the distribution of deep convective precipitation within the TC and, in the majority of the cases, a change in TC intensity. Currently, there are two main conflicting schools of thought on the relationship between lightning activity (mainly cloud-to-ground flashes (CG)] and TC intensity change: The great majority of the above-mentioned works suggest that CG lightning bursts in the eyewall precede an increase in intensity of the system while others (Thomas et al. 2010; DeMaria et al. 2012) have suggested the opposite (i.e., weakening). Pioneering work by Molinari et al. (1999) suggested two possible scenarios: if a TC is already rapidly deepening, eyewall CG burst may precede weakening and vice versa. In light of this contrast of ideas, it is proposed that explicit modeling of the electrification within TCs may provide further insight on some of the key factors behind this complex relationship.

Fierro et al. (2011) performed the first observational study showing a three-dimensional analysis of the lightning activity including both CG and a class of intense intracloud (IC) flash during the intensification phases of three major hurricanes: Katrina (2005), Rita (2005), and Charley (2004). They correlated intensification periods with episodic eyewall IC discharge bursts associated with convective events rotating around the eye and an aggregate increase in IC discharge heights. Furthermore, they found that the evolution of IC discharges was key in helping to distinguish differences in convective regimes occurring in the eyewall during or prior to intensification periods. Their results support previous findings from observations of total lightning within continental deep convective storms whereby total (IC + CG) flashes revealed an excellent correlation with convective strength, in contrast to CG flashes alone (e.g., MacGorman et al. 1989; Lang and Rutledge 2002; Wiens et al. 2005; Schultz et al. 2011).

To date, there have been relatively few modeling studies dedicated to exploring in detail the electrical processes within TCs and their relationships to small-scale convective processes (viz., Fierro et al. 2007, Fierro and Reisner 2011, and Fierro et al. 2013). Little is still known about this physical aspect of the TC, though a better understanding of its nature could help improve short-term forecasts of their potential for intensity changes, both at sea and at landfall. Continuous monitoring of total lightning by the Geostationary Lightning Mapper (GLM; Goodman et al. 2013) on the upcoming Geostationary Operational Environmental Satellite "R" series (GOES-R) in conjunction with lightning data from global lightning networks (e.g., Earth Networks and/or the World Wide Lightning Detection Network; Abarca et al. 2011) potentially offers real-time monitoring of TC intensity changes if the relationships with lightning are robust and better understood.

Although highly idealized (i.e., no terrain and Rankine vortex initialization) Fierro et al. (2007) made use of a 3D stochastic branched lightning model (Mansell et al. 2002, 2005) coupled with a single-moment bulk microphysics scheme with 2 liquid- and 10 ice-phase hydrometeor categories within the Straka Atmospheric Model (SAM; Straka and Mansell 2005) on a 2-km grid. The availability of a wide range of ice species in this model allowed for a broad spectrum of fall velocities and, hence, more realistic representation of in-cloud charge structures (e.g., Saunders and Peck 1998). SAM was able to generate a realistic hurricane with a lightning pattern consistent with those reported by past investigators (e.g., Orville and Coyne 1999; Cecil and Zipser 2002; Cecil et al. 2002). Similar to observations, the eyewall of the simulated TC using SAM was characterized by the production of negative CG flashes. The simulated gross structure resembled a normal tripole (vertical structure of lower positive, main negative, and upper positive charge regions), produced by negative noninductive charging of graupel at midlevels and positive inductive charging near 0°C.

Using the Los Alamos National Laboratory's hurricane model (HIGRAD; Reisner et al. 2005), Fierro and Reisner (2011) presented the first real case modeling study (i.e., with terrain and mesoscale initialization) of

TC electrification at 2-km grid spacing in an attempt to relate intensification phases to the evolution of total lightning activity and the associated presence of eyewall convective events as reported in Fierro et al. (2011). Further improving upon Fierro et al. (2007), this study made use of observed radar and lightning data during the vortex initialization, which produced a simulation of Rita in good agreement with the observed storm. Consistent with observations of Fierro et al. (2011), the model was able to reproduce rapidly rotating electrically active convective events near the radius of maximum wind (RMW) during intensification phases.

This work will build upon the recent modeling works of Fierro and Reisner (2011) and Fierro et al. (2013) by utilizing an arguably more realistic three-dimensional discharge code adapted from MacGorman et al. (2001, hereafter M01) implemented into the Weather Research and Forecasting (WRF) electrification model (E-WRF). In contrast to the approach utilized in Fierro et al. (2013) (viz., Ziegler and MacGorman 1994, hereafter ZM94), M01 constrains the discharge within a cloud volume, characterized by net charge density and the electric potential, and is able to produce three-dimensional flash structures (i.e., flash volumes). In addition to the simulated flash origin densities, the M01 scheme also allows the computation of additional relevant lightning metrics such as flash extent densities (e.g., for GLM) and number of channel volumes. The capability of explicitly forecasting three-dimensional lightning volumes is critical for exploring key relationships between kinematical/microphysical variables and lightning in more detail—for example, via time–height diagrams or contour plot histograms.

Among the chief rationales for acquiring a better understanding of the cloud-scale electrification structures within TCs is the potential to develop physically consistent lightning predictors for the assimilation of lightning data into numerical weather prediction (NWP) models (e.g., Mansell et al. 2007; Fierro et al. 2012, 2015; Marchand and Fuelberg 2014; Mansell 2014) and statistical prediction models (e.g., Kaplan et al. 2010). This capability becomes even more desirable given the upcoming launch of the GLM on GOES-R in early 2016 (Goodman et al. 2013), which will be capable of mapping total lightning (cloud-to-ground + intracloud) day and night, year-round with a nearly uniform resolution ranging between 8 and 12 km over the Americas (Gurka et al. 2006).

2. Relevant aspects of this simulation

It is emphasized that we do not intend in this study to produce a best possible forecast of one particular hurricane in terms of its track or its evolving intensity, structure, and lightning. The general environment and trends of Hurricane Isaac (2012), whose lightning activity was observed by the Earth Networks Total Lightning Network (ENTLN), were used chiefly to produce a generally realistic TC simulation, whose reflectivity structures and lightning behaviors were within the range observed in TCs in the same general region as Hurricane Isaac.

As will be shown later in the results section, despite differing from the observed lightning morphology of Isaac, our simulated lightning pattern lies within the range observed in TCs that evolved in the same general geographical area as Hurricane Isaac. The lightning patterns in our simulation of a category 2–3 hurricane closely resemble those sampled in Hurricane Karl (2010; Reinhart et al. 2014) and Hurricane Paloma (2008; Pardo-Rodriguez 2009). At the time of peak intensity (category 3), both storms were characterized by abundant eyewall lightning with comparatively little lightning in the rainbands. Although the lightning detection systems used in these studies detected mainly cloud-to-ground lightning, while our simulation produces total lightning activity (IC + CG), the average behavior of total lightning probably has the same or similar spatial relationships as CG flashes alone. From what is known about the causes of CG flashes (e.g., MacGorman et al. 2011), there is nothing in the established characteristics of the eyewall and rainband that would favor CG flashes composing a larger fraction of total lightning activity in one region than in the other.

Because the simulated lightning behavior has been readily observed in nature, we believe that an evaluation of the time-dependent model diagnostics of the fundamental interactions between the small-scale kinematic, microphysical, and charging processes and subsequent lightning in the general TC model can provide meaningful insights into the nature of lightning within TCs. The chief goals of this work are to 1) provide an in-depth analysis of the in-cloud electrical structure and evolution of the simulated TC; 2) determine how the simulated electrification relates to changes in the microphysical, kinematic, and structural characteristics of specific regions of the TC to better understand the nature of the electrification within TCs; and 3) determine how the simulated electrical behaviors relate to those observed and simulated within continental storms.

Two of the primary electrical parameters used to address this goal are the total lightning channel volume (LCV) and net charge density. LCV can be viewed as a measure of the total electrical discharge activity by considering flash size (volumetric extent) combined with flash rate. The distribution of net charge is related to

in-cloud conditions such as ambient temperature and supercooled liquid water content (e.g., Takahashi 1978; Jayaratne et al. 1983; Gardiner et al. 1985; Saunders et al. 1991, 2001; Brooks et al. 1997; Saunders and Peck 1998; Emersic and Saunders 2010). For TCs, the gross vertical charge structure was shown to resemble a normal tripole in the eyewall (Black and Hallett 1999; Fierro et al. 2011), defined as a main midlevel negative charge region with an upper main positive region and a lower (usually weaker) positive region.

3. Lightning model

The version of E-WRF used in this study differs from the previous work of Fierro et al. (2013) by using a more realistic three-dimensional scheme for discrete electric discharges and a simple screening layer parameterization; both of which are briefly described below. For the sake of brevity, the reader is invited to consult Fierro et al. (2013) for the details of the original E-WRF.

The discharge process in E-WRF originally used in Fierro et al. (2013) employs concepts adapted from a well-documented bulk lightning model (viz., ZM94). For this work, the arguably more realistic three-dimensional M01 discharge scheme was implemented into E-WRF. Although being three dimensional and resolving the discharge process of individual flashes instead of considering the discharge process as a bulk collective process across the entire simulation domain (ZM94), the M01 scheme is about 3 times more computationally expensive than ZM94 for similar flash origin density rates, and thus remains currently impractical for real-time use.

As in M01, the initiation of a flash occurs wherever the ambient electric field magnitude E_{mag} exceeds a fixed critical breakdown threshold, given here by the vertical profile of Dwyer (2003). An initial explicit channel extends bidirectionally in small steps from the initiation point. The original M01 scheme extended the channel parallel and antiparallel to the electric field vector, but here the channel is constrained to be vertical to simplify parallelization of the code via domain decomposition. This approximation is justified by years of in situ (MacGorman and Rust 1998) and modeling (e.g., Mansell et al. 2002, 2005) work, which found that regions of high electric fields are generally dominated by the vertical component. Extension of each end continues until the field magnitude drops below a given threshold, set here to 90% of the breakdown value, where substantial branching of the channel is assumed to begin. The interpolated values of potential (ϕ_t) and net charge (ρ_t) at the endpoints are used to define the maximum boundaries of the branching regions. As in M01, the algorithm starts from each endpoint and finds adjacent grid points with charge density and electric potential exceeding ρ_t and ϕ_t, respectively, until no more points are found. All the grid points meeting these criteria can participate in the charge redistribution process whereby opposite charge is superposed onto each hydrometeor type proportionately to its total surface area, similar to ZM94. The fraction of charge superposed per discharge is set to 30% [as in Rawlins (1982)]. A drawback of the above procedure is that propagation could stop prematurely and not consider adjacent pocket(s) of charge with magnitudes of charge density and electric potential sufficiently large to also participate in the charge distribution process of the same flash. To account for this possibility, once no more points satisfying the aforementioned criteria (i.e., ρ_t and ϕ_t) for charge redistribution are found, the algorithm then searches for nearby points exceeding a fixed but lower threshold for the electric potential and charge density. These grid points do not participate in the charge redistribution and thus are not counted toward the final positive–negative flash volume count. The sum of the grid points' volumes activated for charge superposition–redistribution and for the flash extension (buffer points) determines the volume of a single hybrid, branched bidirectional flash.

The M01 scheme enforced net neutrality of IC flashes, but this becomes a problem in longer-running simulations because CG flashes are rarely produced by the scheme. An unrealistic net charge can build up in a cell via charge sedimentation to ground and inadequately modeled ion current response. The lightning scheme was therefore hybridized to allow IC flashes to deposit a net charge if it counteracts a net charge in the region of the flash footprint (e.g., allow net negative charge from a flash if the storm column contains net positive charge). CG flashes are rarely produced because, in contrast to an explicit branched lightning scheme (Mansell et al. 2002), M01 does not compute the potential along the channel itself (for propagation against the ambient value). Because the ambient electric field is almost always weak within a potential well (shallow gradient), the initial unbranched lightning channel will rarely extend down near the ground.

For greater computational efficiency, multiple nonoverlapping flashes can be calculated between global solves of the electric potential. Each flash in a group is projected onto a 2D mask array with an added buffer zone of 20 km. Any remaining initiation points outside of the mask can be chosen for another flash, and these flashes are not allowed to overlap previous flashes in the same iteration. Iterations of lightning flashes and solving for the potential continue until no more points satisfy the initiation criteria. Generally, two to three lightning

iterations are required to reduce E_{mag} below the breakdown threshold across the domain.

E-WRF currently does not consider explicit treatment of small ions such as attachment and drift motion (e.g., Chiu 1978; Helsdon and Farley 1987; Mansell et al. 2005). To account for current density discontinuities at cloud top that would occur without ions, a simplified screening layer parameterization following Ziegler et al. (1991) has been implemented. Although the screening layer parameterization of Ziegler et al. (1991) works adequately for isolated clouds, it does not deal as well with complex cloud systems with multiple cloud layers. Thus, the screening layer parameterization was adapted to act only on cloud top, using the vertical components of the electric field below and above the cloud boundary. The charge deposited on the particles at cloud top reduces the electric field just inside the cloud (and, hence, current density).

4. Model physics, grid configuration, and case study observations

a. Model physics and numerics

The numerical cloud model utilized in this study is the three-dimensional compressible, nonhydrostatic WRF-ARW Model (version 3.3.1; Skamarock and Klemp 2008). WRF features several microphysics options, one of which has been adapted to run with full electrification—namely, the National Severe Storms Laboratory's (NSSL's) two-moment microphysics scheme of Mansell et al. (2010). Electrification rates are quite sensitive to the rates of collisions between graupel and smaller ice particles, and the use of a two-moment microphysics scheme allows the particle concentration of all hydrometeor species to be predicted rather than diagnosed. The six bulk species of the NSSL scheme are rain, cloud water, cloud ice, snow, graupel, and hail. Explicit prediction of cloud condensation nuclei (CCN) concentration was activated to reproduce maritime conditions of low CCN concentration (initially a constant $40.8 \times 10^6\,\mathrm{kg}^{-1}$ throughout the domain) and, conjointly, reduce the ice production (Rogers and Yau 1989; Mansell and Ziegler 2013). Khain et al. (2008) also found that predicting aerosols could yield more realistic patterns of ingredients for electrification in the rainbands of a TC in the vicinity of land. Mansell and Ziegler (2013) showed that lower CCN concentration can promote the earlier formation of raindrops at lower altitude and temperature and limits the total latent heat release by condensation with an associated limitation of electrification and lightning rates. Higher CCN concentrations tend to maximize total vapor condensation, increasing the latent heating, peak updraft speeds, drop freezing, and electrification (Rogers and Yau 1989; MacGorman and Rust 1998; Mansell and Ziegler 2013). Droplet size and concentration (directly related to CCN) also affect the production of small ice crystals in the rime splintering process (Mossop 1976; Marks and Houze 1987; Heymsfield et al. 2005, 2006, 2009), which has substantial consequences for electrification via collisions between large and small ice particles (Black and Hallett 1999; Mansell and Ziegler 2013). Because of relatively lower CCN concentrations over ocean [$\sim$(50–100) cm^{-3}]; Rogers and Yau (1989), tropical updrafts (e.g., Heymsfield et al. 2005; 2009) and tropical cyclones (Marks and Houze 1987; Heymsfield et al. 2006; Black and Hallett 1999) are mostly glaciated at temperatures lower than -10°C, with most of the raindrops and liquid water confined below the altitude of the -5°C isotherm. Because these typical maritime storm characteristics were simulated well when using their microphysics scheme with CCN concentrations typical of maritime regions, Mansell and Ziegler (2013) suggested that their microphysics scheme (essentially the same as the version used here in WRF) is appropriate for both continental and maritime tropical convection.

Similarly, there is no evidence that the electrification process itself is fundamentally different for tropical maritime storms than for continental storms, although known dependencies on properties such as ambient temperature, particle size, and supercooled liquid water (droplet) content (e.g., Takahashi 1978; Saunders and Peck 1998; Saunders et al. 1991, 2001; Brooks et al. 1997; Avila et al. 1998) are expected to cause some different outcomes. This indicates that it is appropriate to use the electrification parameterizations described in the previous section for simulations of tropical storms. Thus, as long as there are suitable microphysical conditions, in-cloud electrification is expected to occur whether in hurricane convection or continental storms and, in fact, can occur to some extent even in convective clouds not producing any lightning.

A similar argument supports the lightning parameterization. The chief role of a lightning discharge is to dissipate energy by redistributing (depositing) charge to reduce the local electric field, independent of the microphysics and kinematics that produced the field. The principles of physics upon which the discharge parameterization of M01 was based were effectively supported by the fundamental, more detailed physics in the branched lightning scheme of Mansell et al. (2002, 2010). As hypothesized by MacGorman et al. (1981) and demonstrated by Williams et al.'s (1985) experiments with sparks in plastic blocks doped with regions of charge and by Coleman et al.'s (2003) simultaneous observations of lightning and electric potential,

lightning tends to propagate into and remain within electric potential wells, which tend to lie within regions containing charge. M01 and Mansell et al. (2002, 2010) demonstrated that their parameterizations of lightning replicate this behavior, as we would expect. Again, there are no known physical differences between continental and maritime tropical lightning, other than the variations arising from the specifics of the charge structure that are caused by variations in the microphysical and kinematic properties of the storms and storm systems; the fundamental physics governing the electrical processes and encapsulated in our parameterizations are the same. Electrification and lightning are governed by the same physics in the eyewall and in the rainband convection, and this allows us to begin to examine the impact of known differences in the microphysical and kinematic characteristics between the two regions on lightning activity.

The remainder of the physics options employed in this study are identical to those of Fierro et al. (2013). The boundary layer is parameterized following the Eta-model implementation of the 1.5-order closure Mellor–Yamada scheme (Mellor and Yamada 1982) and the turbulence kinetic energy scheme adapted by Janjić (1994) with Monin–Obukhov–Janjić similarity theory for the subgrid-scale turbulence processes (Chen et al. 1997). Lower boundary conditions for turbulent fluxes are provided by the unified Noah land surface model (Chen and Dudhia 2001; Ek et al. 2003). The longwave and shortwave radiation are both parameterized following the Goddard scheme [adapted from Mlawer et al. (1997)]. As indicated in Fierro et al. (2013), sedimentation and advection of space charge is treated in an identical manner to that of the predicted scalars, which employ the fifth-order weighted essentially nonoscillatory (WENO) scheme (Jiang and Shu 1996) in the vertical and horizontal, with a positive-definite limiter added for moisture scalars. Sedimentation for particle mixing ratio, number concentration, and charge employ a first-order upwind scheme. Charge sedimentation uses the appropriate mass-weighted fall speed of the hydrometeor species.

b. Model domain and grid nesting

The simulation domain (Fig. 1) consists of a parent domain with a uniform horizontal grid spacing of 1050 m (D01) that contains a vortex-following inner nest (e.g., Michalakes et al. 2005), with a uniform horizontal grid spacing of 350 m (D02). The grid resolution of D02 is desirable to better resolve the characteristic width of tropical updrafts and some of the transient, small-scale convective processes within the eyewall of the TC (Bryan et al. 2003; Fierro et al. 2009a; Rotunno et al. 2009; Davis et al. 2010).

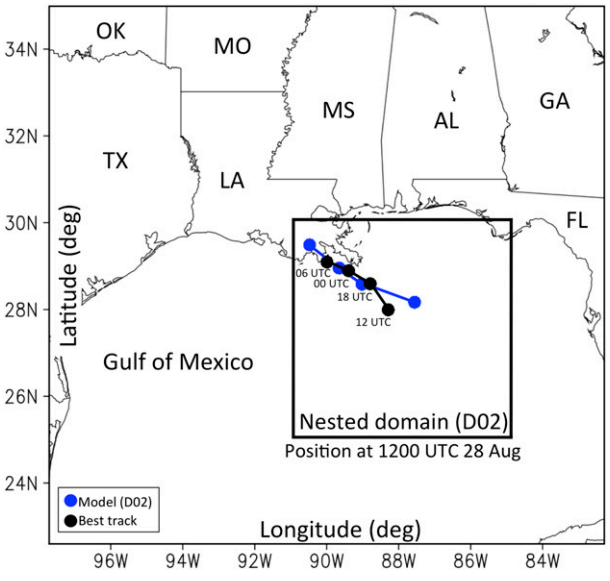

FIG. 1. Sketch of the 1050-m parent domain (D01) and of the 350-m inner-moving nest (D02) at its initial location at 1200 UTC 28 Aug. The simulated 6-hourly track of the hurricane within the inner nest is shown in blue with the observations from the best-track dataset shown in black (made publicly available by the National Hurricane Center: http://www.nhc.noaa.gov/data/). States are indicated by their usual abbreviations and the legends for colors and shadings are shown at the bottom left.

The chosen horizontal grid dimensions are 1430 × 1320 (D01) and 1714 × 1714 (D02), respectively, yielding a horizontal inner grid size of 600 × 600 km^2, which is sufficient to capture a sizeable fraction of the outer rainbands. To better resolve boundary layer processes, the stretched vertical grid has 71 levels with a domain top set at 50 hPa (i.e., ~20 km). The computational time steps on the parent domain and inner nest are set to 6 and 2 s, respectively. The initial and time-dependent lateral boundary conditions employ the 3-hourly, 12-km North American Mesoscale (NAM) Model forecast data for a 30-h period starting at 0000 UTC 28 August 2012. To allow for the incipient vortex to reasonably spin up, D02 was spawned 12 h into the simulation—specifically, at 1200 UTC 28 August 2012 (Fig. 1). To reduce computational burden, electrification only was activated on the inner nest. Owing to the prohibitively large size of individual raw output files (i.e., ~50 GB for D02), the output data were saved every 3 h on D01 and every hour on D02.

c. Constrained model solution via continuous lightning data assimilation

As will be shown later in the analysis, the vast majority of the observed lightning in Isaac occurred in the rainbands. Thus, to better represent deep convection in the simulated rainbands, the lightning data provided by the

ENTLN were continuously assimilated throughout the 18 h of simulation on the storm-following inner nest [similar to Fierro and Reisner (2011)]. Weakly constraining the model solution via continuous lightning data assimilation makes the simulated convection more realistic and provides simulated TC fields to facilitate model-based analyses of the relationships between simulated kinematics, microphysics, and electrification.

The assimilation procedure follows the methodology of Fierro et al. (2012). The lightning data first were binned into 1-h increments and projected onto a 350-m-resolution, $600 \times 600\,km^2$ domain (same dimensions as in D02) with the geographical coordinates of this domain corresponding to the coordinates of D02 at the end of the assimilation interval. The $350 \times 350\,m^2$ ENTLN densities were projected onto an assumed pseudo-GLM footprint resolution of $9 \times 9\,km^2$ (in addition to using a 1-h binning interval). This differs from Fierro et al. (2012), who utilized a 10-min interval to assimilate lightning in their tornado outbreak case and in their severe continental mesoscale convective system derecho case (Fierro et al. 2014). The rationale for this procedure is motivated by Fierro and Reisner (2011), who employed a 3-h binning interval to assimilate CG data from the Los Alamos Sferics Array (LASA; Shao et al. 2006) network to improve the representation of the rainbands within Hurricane Rita (2005). Using a longer assimilation interval coupled with a larger footprint for the lightning densities than was used for continental storms is necessary to produce a significant effect on the convective cells in the rainbands, which have a smaller characteristic length scale and typically exhibit much smaller flash rates (e.g., Petersen et al. 1996, 1999; Williams and Stanfill 2002).

d. Case study and observational data used to evaluate the model

In this work, emphasis will be directed toward Hurricane Isaac (2012), which evolved over the Gulf of Mexico and made a U.S. landfall in Louisiana. Isaac's eyewall featured a time window of about 24 h within 1000 miles of the U.S. coast during which the ENTLN detection efficiency was ~(40%–50%) for ICs and over 95% for CGs [see Fig. 6 in Fierro et al. (2012)]. From 2009 to 2013, only two hurricanes besides Isaac (2012) have made landfall in the United States, namely Hurricanes Irene (2011) and Sandy (2012). Isaac was selected because the ENTLN detection efficiencies and location accuracies along the track of the storm during the 18-h period of interest in this work were overall superior than for Irene or Sandy. This is because in 2012, the ENTLN featured a relatively higher density of sensors in east Texas, Florida, and southern Alabama [see Fig. 6 in Fierro et al. (2012)].

The sources of the datasets used for model evaluation are as in Fierro et al. (2012). The observations of radar reflectivity fields employ the three-dimensional National Mosaic and Multisensor Quantitative Precipitation Estimation (QPE) product from NSSL (referred to as NMQ; Zhang et al. 2011). The horizontal grid spacing of the NMQ dataset is 0.01° and the vertical grid spacing stretches from 250 m between $z = 500$ m and 3 km AGL, to 500 m between $z = 3$ and 9 km, and to 1 km above it until 18 km.

The simulated lightning flash origin densities will be evaluated against the total lightning data from the ENTLN broadband (1–12 MHz) network. Over the geographical area covered by the moving inner nest, which extends from southeast Louisiana to about 800 km offshore (see Fig. 1), the location accuracy of ENTLN in 2012 varied from ~300 to 400 m [Fig. 6 in Fierro et al. (2012)]. In this particular geographical area, the detection efficiency for typical CG return strokes (10 kA) exceeded 90% and ranged between 40% and 60% for typical IC flashes (1 kA) [see Fig. 6 in Fierro et al. (2012)]. Given a typical IC:CG ratio of 2:1 (Boccippio et al. 2001), it is reasonable to assume that ENTLN detected, on average, about half to two-thirds of the total lightning within Hurricane Isaac (2012) that occurred during the 18-h period covered by this analysis.

5. Results

a. Comparisons with observations

Although this study does not aim at generating the best possible forecast of a particular hurricane (here, Isaac), it is relevant to first evaluate the performance of the model in reproducing some basic morphological features of TCs in D02 prior to engaging in the analysis of the evolution of the simulated electrical fields. The rationale for not focusing on the details of this TC is that, based on additional simulations and previous electrification modeling work (Mansell et al. 2002, 2005, 2010; Fierro et al. 2006, 2007, 2008, 2013; Fierro and Reisner 2011; Kuhlman et al. 2006; Calhoun et al. 2014), the salient relationships derived herein between simulated electric variables and kinematics–microphysics fields are expected to remain similar for any given TC simulated with this lightning model. This is because, as indicated in section 4a, electrification and lightning in the eyewall and in the rainband convection are governed by the same physics. Details of the simulated electrification, however, such as the vertical arrangement of charge, flash polarity, and flash rates can be affected by (i) the microphysics scheme, (ii) CCN concentration–prediction, and (iii) the specifics of the selected noninductive charging scheme. Hence, while it is

possible to produce a storm in better agreement with the observations, in terms of intensity and general structure, through more sophisticated data assimilation techniques (e.g., Aksoy et al. 2009; Gao et al. 2013), the latter will not affect the main relationships with the simulated electrification herein. Last, as indicated in section 2, the simulated lightning pattern herein lies within the range of observed patterns within TCs in this general geographical region (e.g., Hurricanes Karl or Paloma).

The simulated track remains generally aligned with the "Hurdat2" best-track data from the National Hurricane Center (NHC; Landsea and Franklin 2013) with the simulated storm tracking generally faster than observed and initially showing a southeastward bias (Fig. 1). Although the simulated minimum surface pressure agreed reasonably well with the observations initially (1200 UTC 28 August), the simulated storm undergoes overall a sharper-than-observed deepening rate with a maximum difference in minimum surface pressure reaching ~10 hPa at 0400 UTC 29 August near the end of the simulation (Fig. 2b). Concurrently, the simulated maximum 1-min sustained winds at 10 m exceed the best-track observations by as much as 15 m s^{-1} (not shown).

Despite a more intense storm overall, the range of simulated storm-total flash rates remained generally comparable to the observations, with simulated rates (excluding the electrification spin up during the first hour) generally ranging between 300 and 1300 h^{-1} and the observed rates ranging between 20 and 1300 h^{-1} (Fig. 2). This result holds if one considers that ENTLN detects about half to two-thirds of all the flashes, as indicated in the previous section. Despite a comparable range of storm-total flash rates, the evolution of the simulated flash rates exhibits some stark differences with the observations: for example, the simulated flash rates in the eyewall are much larger than observed by as much as two orders of magnitude (cf. Figs. 2a and Fig. 2b). Conversely, the simulated flash rates in the rainbands are underestimated by as much as a factor of 10. Moreover, the model produces a lower degree of variability in flash rates than was observed. As might be expected from the unpredictability of moist convection within TCs (Zhang and Sippel 2009), the timing in the simulated peak flash rates and convective pulses in both the eyewall or the rainband regions generally does not coincide with the observations. Furthermore, the bulk of the simulated flashes were produced in the eyewall, in stark contrast to the observations, which had almost all flashes in the rainbands. From ~0100 UTC until the end of the simulation at 0600 UTC 29 August, the modeled flash rates exhibited the largest departure from the observations: while the model produces an overall decreasing trend in its total rates, the observations show the opposite.

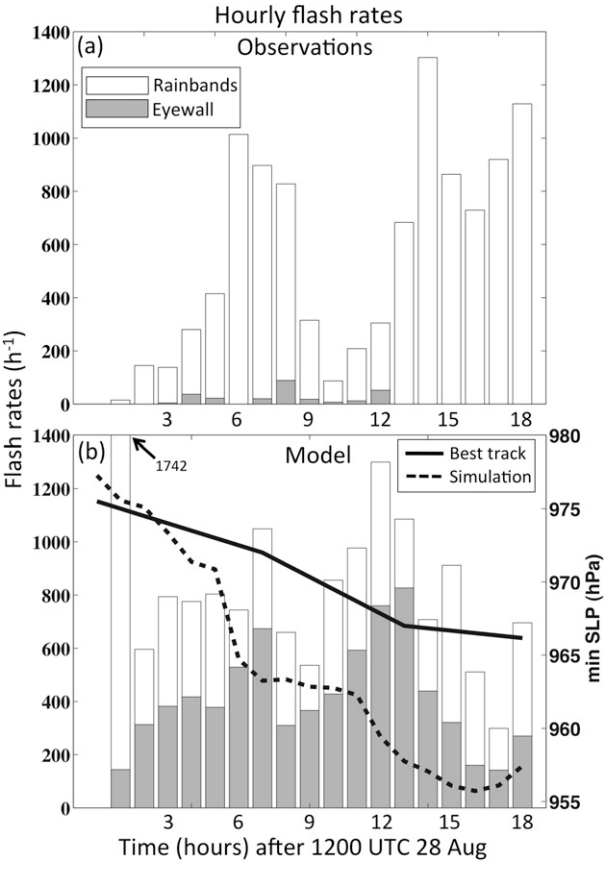

FIG. 2. Time series of the hourly flash rates for (a) the ENTLN observations and (b) the simulation. The simulated flash rates were computed within the 600 × 600 km^2 inner nest (D02; see Fig. 1) with the observations using a 6° × 6° domain instead (i.e., 1 km ≈ 0.01° is assumed). The storm center in the observations was determined using the best-track data. The total hourly flash rates were subdivided by the rainbands (white bars) and eyewall (gray bars) regions. Eyewall flash rates include all flashes within a 100 × 100 km^2 box. The sum of the white and gray bar flash rates is the "storm total" rate, which is shown on the left axis. To facilitate comparison between (a) and (b), the scale for the flash rates is the same in both panels. Also displayed in (b) is the simulated hourly pressure trace (dashed line) and the 6-hourly pressure trace estimate from the NHC best-track data (thick black line; hPa). The time axis shows the time in hours after 1200 UTC 28 Aug when D02 was initialized. Because the first hour of accumulated lightning data in the model starts at 1300 UTC 28 Aug, the observed flash rates accumulated up to 1200 UTC 28 Aug were intentionally left blank. Because the simulated total flash rates during the spinup period (first hour) remained relatively larger, its value (1742) is indicated by an arrow in the top-left corner in (b).

Bearing in mind, again, that this simulation should be viewed as generic in terms of electrification within TCs and not intended to reproduce the particular convective and electrical behavior of one particular hurricane, it is relevant to note two periods of relatively larger

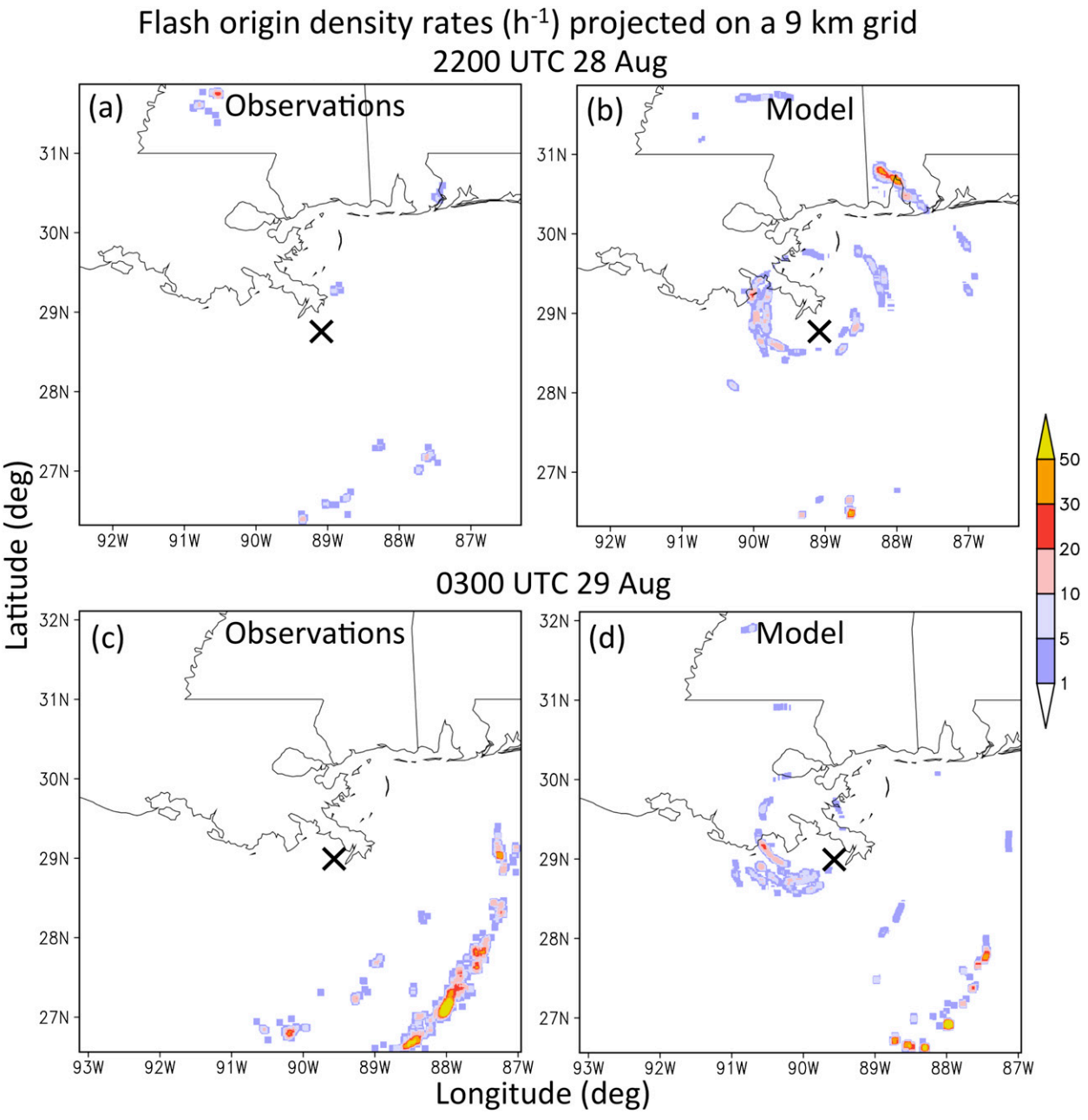

FIG. 3. Horizontal cross section of hourly flash origin density rates for the ENTLN observations at (a) 2200 UTC 28 Aug and (c) 0300 UTC 29 Aug; and (b),(d) for the simulation at the same times, respectively. The simulated and observed flash origin density rates both are displayed on a pseudo-GLM-resolution 9-km grid within the storm-centered 600 × 600 km^2 inner-nest domain to facilitate the comparisons. The observations in (a),(c) are shown on the inner nest because, incidentally, these also display the flash origin density fields that are assimilated during the hourly interval starting at the times shown in (b),(d), respectively. For reference, the location of the observed storm center is denoted by an × symbol.

deepening rates in the simulation, namely 1700–1800 UTC 28 August and 2300 UTC 28 August to 0000 UTC 29 August. Both of these are coincident in time with a relative increase in eyewall flash rates (Fig. 2b), reminiscent of the behavior documented in many studies (e.g., Fierro et al. 2011).

Figure 3 illustrates how the differences between simulated and observed eyewall–rainband flash rates in Fig. 2 translate in the horizontal on an assumed pseudo-GLM-resolution 9-km grid (to facilitate comparison). Observations indicate that during the 18-h time window of this analysis, Isaac produced the bulk of its lightning within the

rainbands located in the south-southeast quadrant (Figs. 3a,c). The pseudo-GLM flash origin density rates within these rainbands peaked at and after 0000 UTC 29 August with values often exceeding $50\,h^{-1}$ (Fig. 3c) with the simulation producing overall comparable maximum rates in the rainbands, although with smaller area (Figs. 3b,d).

Comparing the observed and modeled reflectivity helps to better understand the aforementioned contrasting behavior of simulated and observed eyewall and rainband lightning rates. The eye remained too far offshore to be completely sampled by the Weather Surveillance 88-D coastal radars (particularly, KLIX and KMOB) prior to ~0000 UTC 29 August (Fig. 4). The observed reflectivities at 4 km MSL in Isaac's eyewall seldom exceed 45 dBZ, in contrast to the model, which consistently overestimates the reflectivity maxima by as much as 15 dBZ (Figs. 4a,c versus Figs. 4b,d). The tendency for cloud models to overestimate radar reflectivity within the eyewall of TCs has been well documented over the years by several investigators (e.g., Rogers et al. 2007; Fierro et al. 2009a). These studies hypothesized that discrepancies between simulated and observed dBZ fields partly arose from errors in the microphysics such as terminal fall speeds, reflectivity–mass relationships, intercept parameter, and assumed particle densities. Although observations of vertical velocities were not available for Isaac during this analysis period, it is also possible that the simulation may have locally overestimated updrafts in the eyewall and, consequently, graupel mass. Vertical azimuthally averaged profiles of the simulated vertical velocity field, however, reveal values generally not exceeding $2\,m\,s^{-1}$ in the eyewall, consistent with observations in Atlantic hurricanes (Black et al. 1996). In line with a generally stronger storm in the model, the simulated location of maximum winds (and, thus, RMW) is smaller than suggested by the H*Wind analysis (Powell et al. 1998; Stern and Nolan 2009).

The differences in convective structure may also partly arise from errors in the large-scale environment within the initial conditions derived from the NAM dataset and from errors in the model. Although their respective locations relative to the observations generally differ, the simulated rainbands show two distinct structural modes (e.g., Houze 2010; Didlake and Houze 2013) with either a succession of discrete convective cells or wider bands of moderate [~(40–45) dBZ] reflectivities connecting to the eyewall (e.g., eastern semicircle in Fig. 4d) that mainly are associated with melting snow (see later in the analysis). Despite this broad agreement in rainband reflectivity structure between the model and observations, the model produces smaller flash rates in the rainbands. As will be shown later in this section, this is related to overall larger reflectivities and deeper echo tops in the observed outer rainbands.

To provide a more comprehensive view of the evolution of the lightning activity and reflectivity fields during the 18-h analysis period, Hovmöller diagrams of 4–7-km-layer-averaged observed and simulated reflectivity fields overlaid with azimuthally averaged flash origin density rates were constructed (Fig. 5). The flash origin density rates in the observations appear much larger than the simulation partly because the native resolution of the NMQ data (0.01°) wherein the ENTLN data were projected onto a grid that is a factor ~3.5 larger than the model (350 m). Consistent with the results drawn from selected times (Fig. 4), the model tends to produce larger-than-observed axisymmetric reflectivities in the eyewall by as much as 20 dBZ (e.g., Rogers et al. 2007; Fierro et al. 2009a; Gentry and Lackmann 2010). The smaller azimuthally averaged eyewall reflectivities in the observations (Fig. 5a) further are exacerbated by a generally asymmetric opened eyewall (Figs. 4a,c) compared to a generally more axisymmetric closed eyewall in the simulation (Figs. 4b,d), particularly in the last 10 h of simulation. These differences are consistent with a stronger TC in the model (Fig. 2). As the simulated storm intensifies, the RMW contracts from about $R = 105$ to 45 km (Fig. 5b; e.g., Stern and Nolan 2009). Owing to the aforementioned eyewall asymmetries (Fig. 4), the more diffuse observed axisymmetric projection of eyewall reflectivities makes it difficult to properly estimate the radius of the eye (Fig. 5). Looking at individual horizontal cross sections at these altitudes (e.g., Figs. 4a,c), however, it appears that the radius of the observed eye exhibited noticeable variability and ranged between about $R = 50$ and 120 km with the simulated eye ranging from about $R = 80$ km at the beginning of the simulation to about $R = 50$ km at the end (Fig. 5). Overall, the simulated flash origin densities are well collocated with the azimuthally averaged 6–10-km-layer-averaged vertical velocity contours of $0.5\,m\,s^{-1}$ (Fig. 5b), which also contract as the storm intensifies.

Azimuthally averaged vertical profiles of radar reflectivity fields provide additional clues on the factors behind the contrasting lightning behavior documented earlier between the observations and the model (Fig. 6). At both times, the model produced deeper reflectivity contours in the eyewall with the 30-dBZ echoes reaching altitudes well above the top of the mixed-phased region—defined throughout the paper as the layer between 5 and 7 km or between about 0° and −20°C—in contrast to the observations with 30-dBZ tops seldom exceeding 6 km (Figs. 6a,b and Figs. 6c,d). The departure from the observations becomes more pronounced as the simulated eyewall becomes more axisymmetric in the later half of the simulation (Fig. 4d), with the simulation exhibiting echoes reaching progressively higher altitudes along

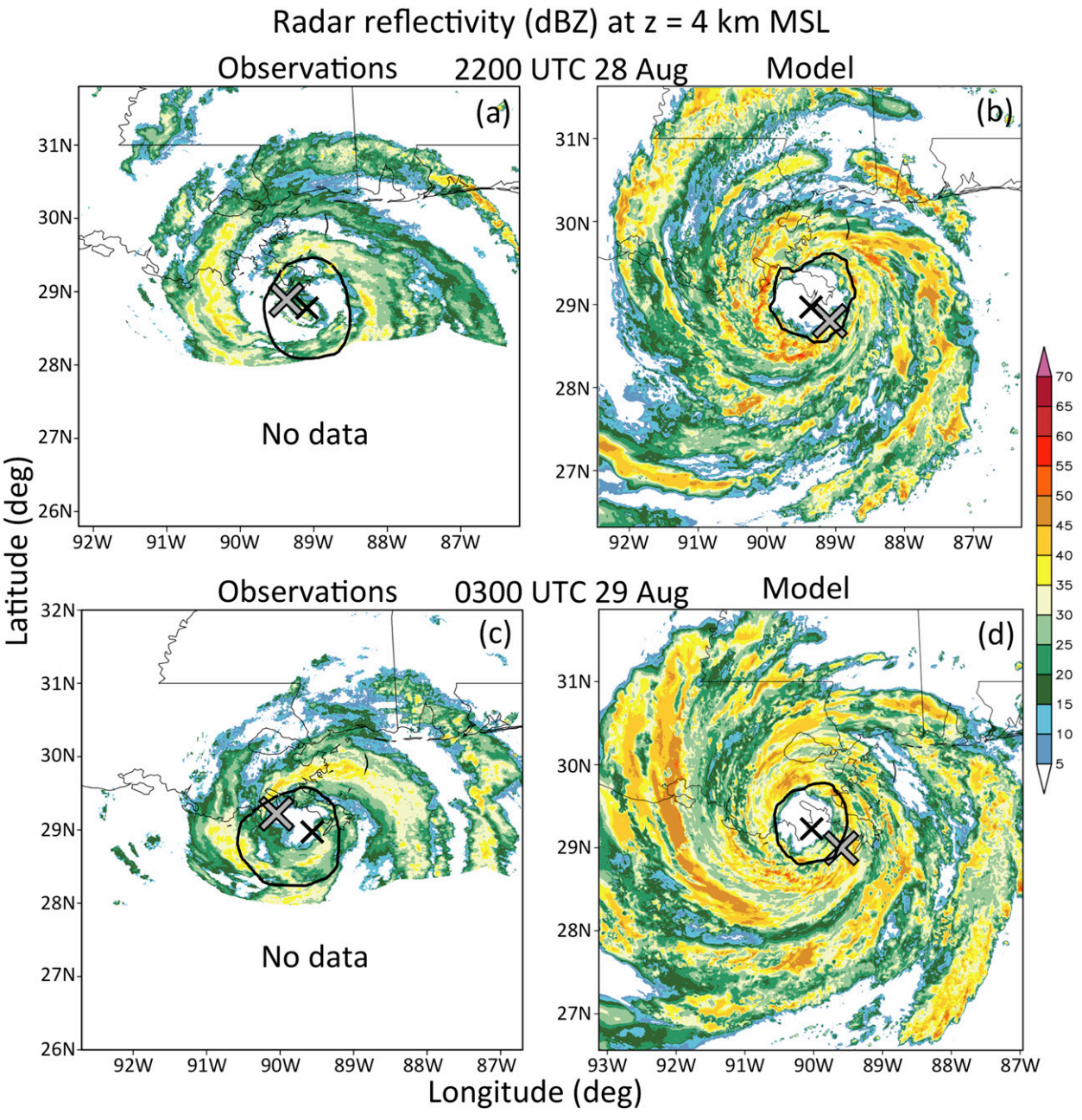

FIG. 4. As in Fig. 3, but for the radar reflectivity fields at $z = 4$ km. Also, in contrast to Figs. 3a and 3c, the observations in (a),(c) are shown in a storm-centered domain relative to the best-track data from NHC. Because the NMQ radar observations are provided on a 0.01° grid, these are shown on a 6°× 6° domain in (a),(c) [instead of a 600 × 600 km^2 domain for the model in (b),(d)]. The thick black closed contour in each plot delineates the approximate location of the maximum horizontal winds (RMW) near the surface. For the observations, the data from the H*Wind project at the Hurricane Research Division (Powell et al. 1998) were perused to estimate the location of maximum horizontal winds. The black × denotes the center of the storm in the analysis domain at the time shown, which by definition lies at the center of the domain. For convenience, a larger gray filled × symbol also shows the respective location of the storm center in the observations and in the model in (a),(c).

with the appearance of larger azimuthally averaged reflectivities (Figs. 6c and 6d). At radial distances beyond $R = 200$ km, the reflectivities in the model rarely exceed 25 dBZ below the freezing level (Figs. 6b,d), in contrast to the observations. Consistent with simulated higher echo tops, the model produces a well-defined bright band, which is not seen in the observations. The simulated eyewall slope as measured from the vertical axis is also

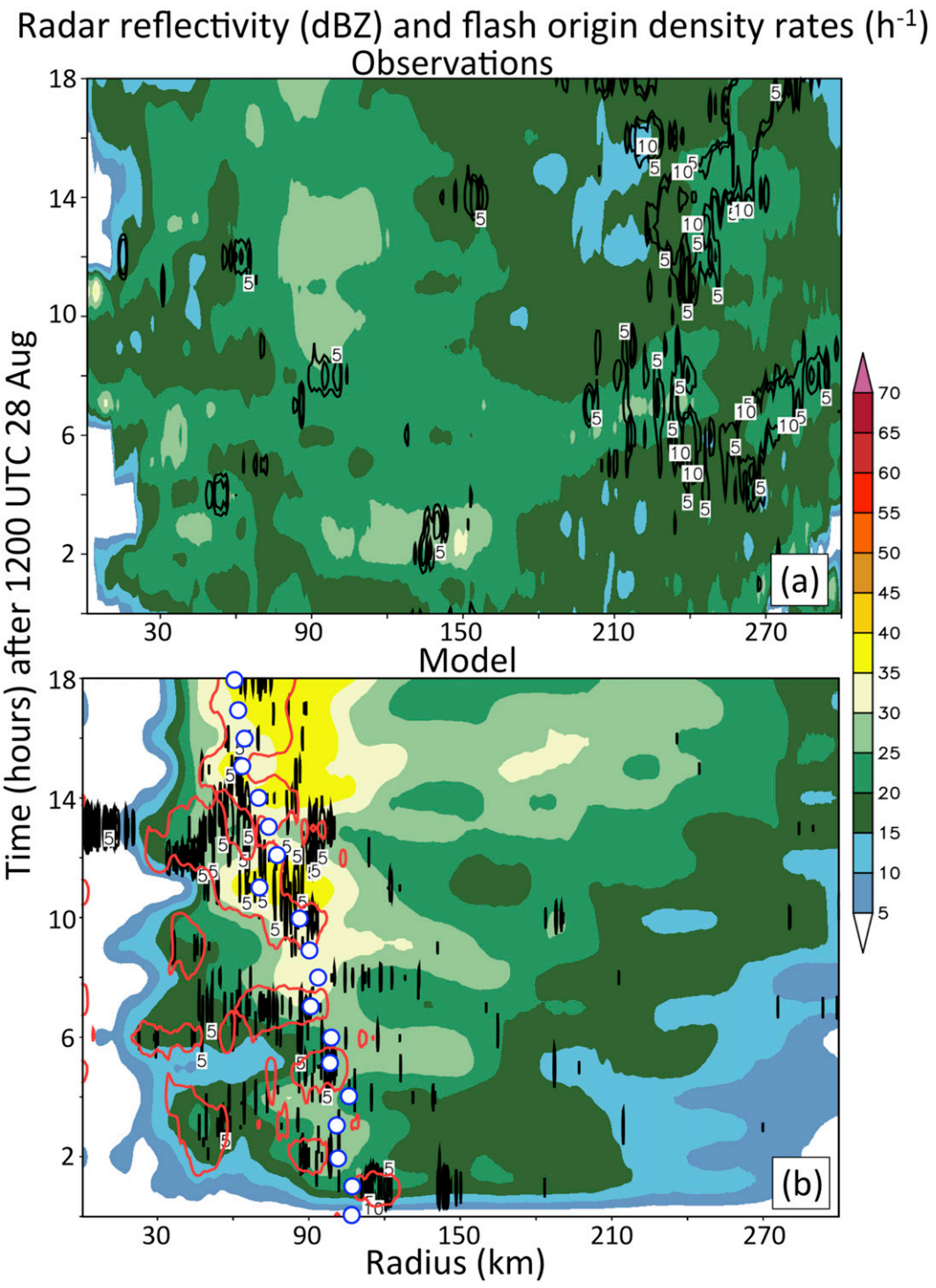

FIG. 5. Storm-centered Hovmöller diagrams of the radar reflectivity fields averaged within the $z = 4$–7-km layer and overlain with the 5- and 10-hourly flash origin density rate contours multiplied by a factor of 1000 for (a) the observations and (b) the model. Note that the flash origin density contours appear thinner in the x directions in (b) compared to (a) because the native grid spacing of the model is 350 m, compared to 0.01° for the NMQ observations. In the observations, grid points with no reflectivity data (owing to radar beam elevation) were not accounted for in the azimuthal average. For convenience, it was assumed for the labels on the x axis in (a) that 1 km ≈ 0.01°. For the model in (b), the 0.5 m s^{-1} 6–10-km-layer-averaged vertical velocity contours are shown in red along with the RMW in white circles.

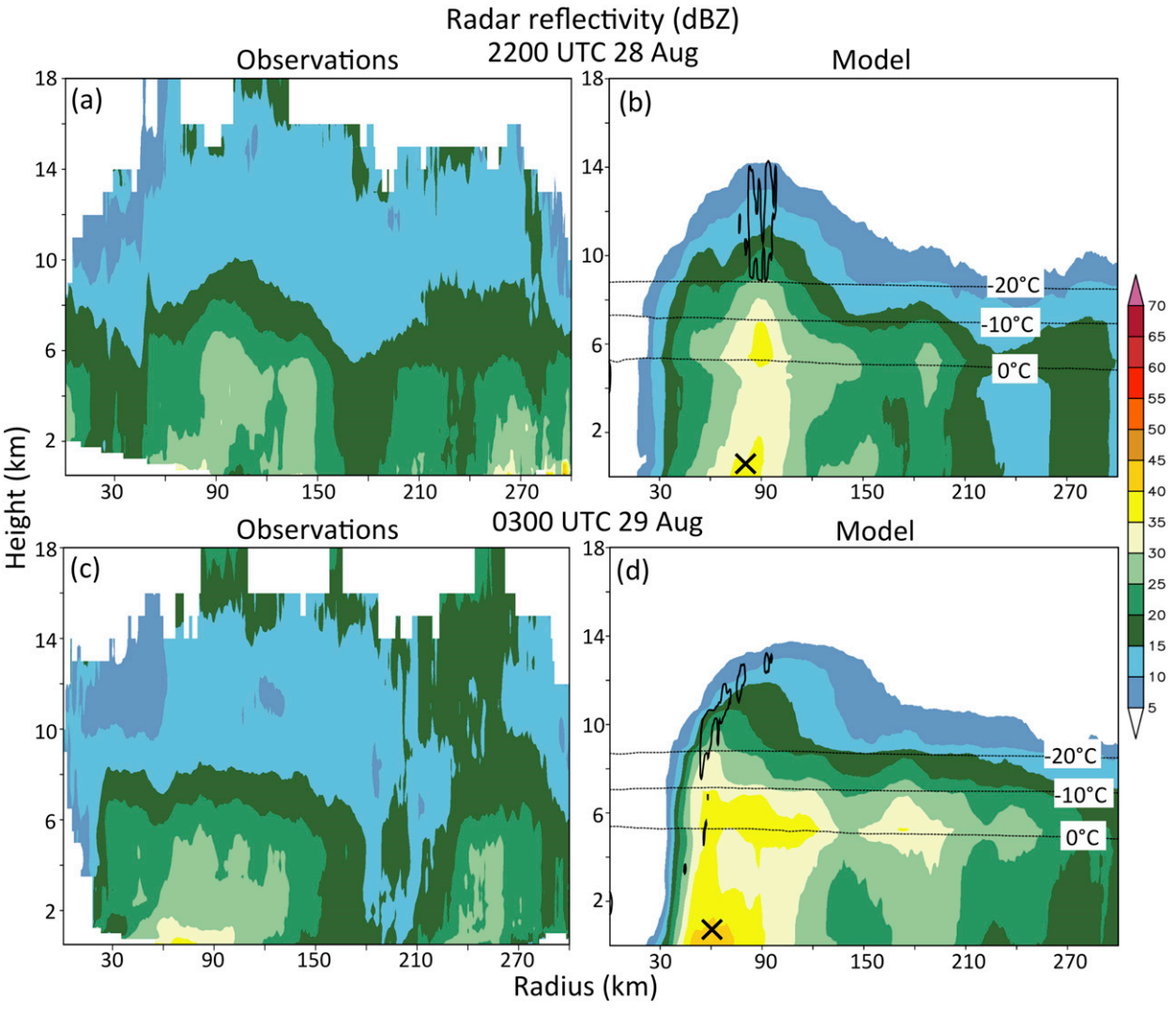

FIG. 6. Storm-centered radius–height diagrams of azimuthally averaged radar reflectivity fields for the observations at (a) 2200 UTC 28 Aug, (c) 0300 UTC 29 Aug, and (b),(d) for the simulation at the same times, respectively. For the simulation, the radar reflectivity is overlaid with the azimuthally averaged 0°, −10°, and −20°C isotherms, which is representative of the electrically active mixed-phase region. As in Fig. 5, points with no data in the observations were not used toward the averaging. Locations in the observations with no data in the azimuth were left blank in (a),(c). As in Fig. 5a, it was assumed for the labels on the x axis in (a) that 1 km $\approx 0.01°$ for convenience. For the model, the RMW near the surface is highlighted by a black × in (b),(d) along with the azimuthally averaged vertical velocities contour of 1 m s^{-1} in black.

generally slightly larger than observed. For example, the simulated slope of the 25-dBZ contour below the freezing level (5 km) at 0300 UTC 29 August is about 70° compared to about 65° in the observations. Consistent with past modeling studies on tropical convection (Fierro et al. 2008, 2009b) and TCs (Rogers et al. 2007; Fierro et al. 2009a), maximum updraft speeds are found in the eyewall near the RMW, well above the mixed-phase region, and are collocated with maxima in 30-dBZ echo tops (Petersen et al. 1999).

Height–frequency reflectivity profile diagrams [e.g., Fig. 5 in LeMone and Zipser (1980)] provide additional information on the structural differences between the observed and modeled eyewall (Fig. 7). Note that the observed frequencies are largely underestimated below $z = 1.5$ km owing to the elevation of the radar beam. In accord with the above analysis, the model consistently produces higher frequencies at larger reflectivities with the observations essentially characterized by negligible frequencies (<2.5%) at reflectivities exceeding 35 dBZ (Figs. 7a,c and Figs. 7b,d). The reflectivity bright band documented earlier in the simulation is manifested by relatively larger frequencies in the 35–45-dBZ bins between 5 and 6 km MSL (Figs. 7b,d). Because of the

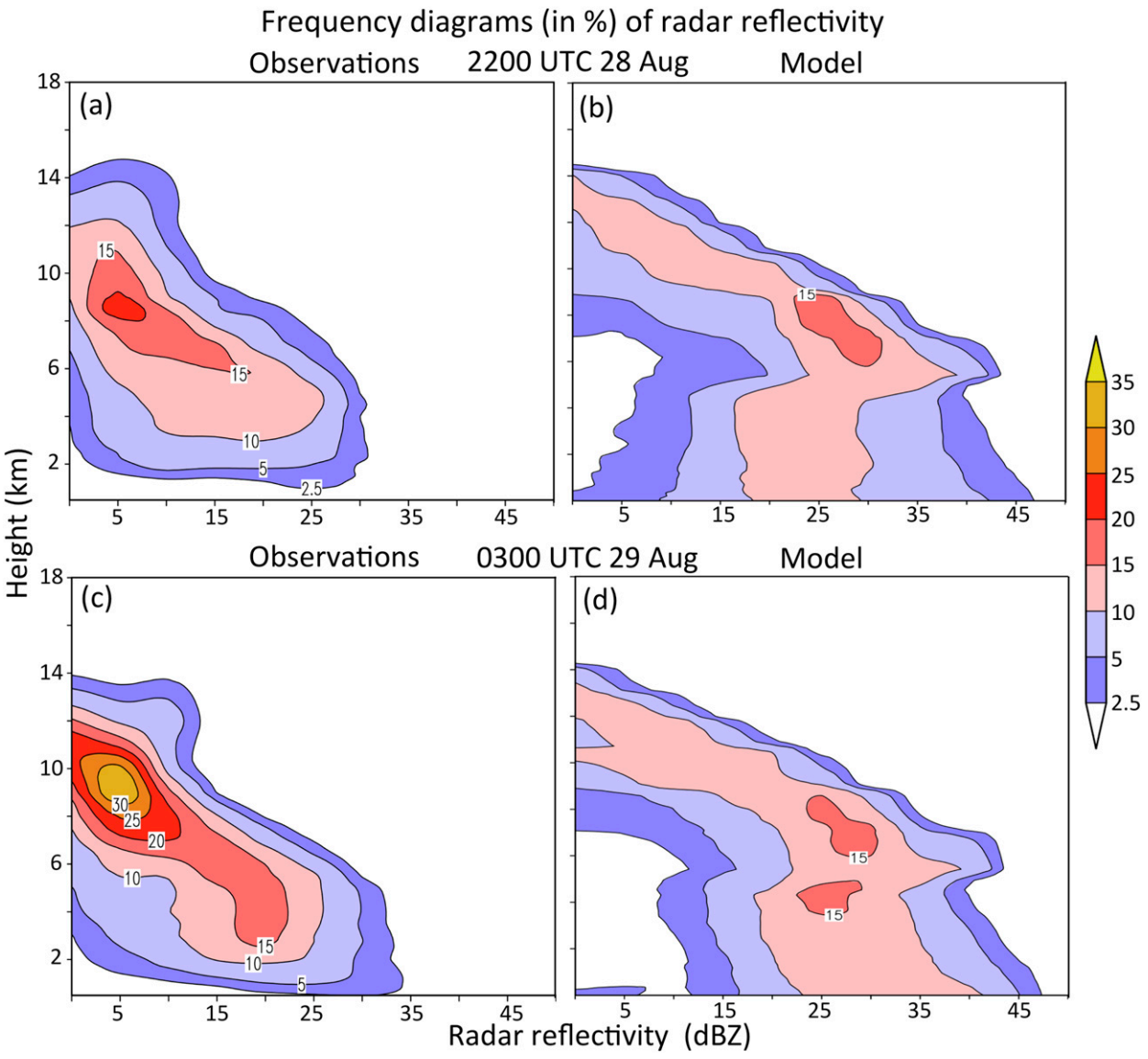

FIG. 7. Contour-frequency diagrams of radar reflectivity in the eyewall region for the observations at (a) 2200 UTC 28 Aug, (c) 0300 UTC 29 Aug, and (b),(d) for the simulation at the same times, respectively. The eyewall region is defined as a storm-centered cylinder of radius $R = 100$ km (1°) in the model (observations). Owing to a data void resulting from the elevation of the radar beam, the frequencies at low levels (below ~1.5 km AGL) in the observations are biased toward small, often near 0, values.

relatively larger reflectivities in the bright band, the model produces a sharper decrease in relative frequencies with height above the freezing level (e.g., Liu et al. 1997; Rogers et al. 2007; Fierro et al. 2009a). Consistent with an observed eyewall characterized by reflectivities seldom exceeding 40 dBZ at $z = 4$ km (Figs. 4a,c) and being largely composed of stratiform precipitation, the 10% frequency contours do not exceed 25 dBZ at and above that level in the observations (Figs. 7a,c). Such frequency distributions are consistent with the composite frequencies of stratiform regions within the eyewall of two hurricanes in Rogers et al. (2007) (their Fig. 7c). In their observations, the largest frequencies are centered at ~25 dBZ at $z = 4$ km compared to ~20 dBZ herein at that level. Except between $z = 4$ and 8 km, where modal frequencies are generally larger in this simulation owing to the bright band, the simulated frequency profile is similar to the stratiform composite of Rogers et al. (2007, their Fig. 7d). Supporting the stratiform nature of the eyewall region of this category 2 storm, the maximum frequencies between $z = 4$ and 10 km are at smaller reflectivities overall than the composites of the category 4–5 TCs presented in Hence and Houze (2011).

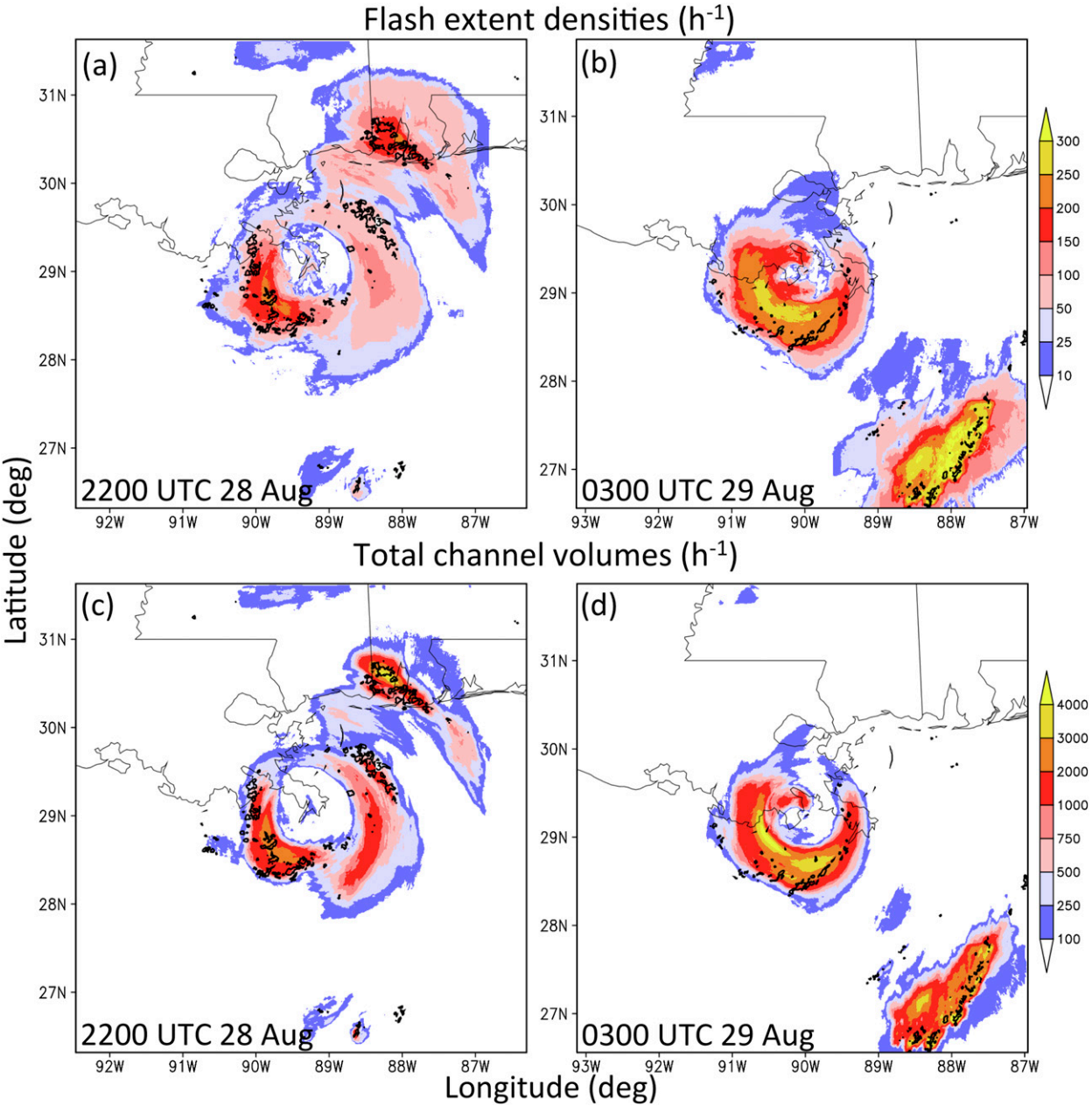

FIG. 8. Horizontal cross section of simulated hourly flash extent densities at (a) 2200 UTC 28 Aug and (b) 0300 UTC 29 Aug. The small thick black contours show the 8–12-km-layer-averaged vertical velocities of 3 m s^{-1}. (c),(d) As in (a),(b), but for the hourly total channel volumes. Legends for colors and shadings are shown on the right of each corresponding row.

b. *Electrical structure*

In addition to flash rates and flash origin density rates (Figs. 2 and 3), the model computes flash extent density rates (Figs. 8a,b) and LCV rates (Figs. 8c,d). The discharge model calculates three-dimensional fields of positive and negative LCVs at each time step. The total LCV is calculated in each grid column by vertically integrating all individual channel unit volumes regardless of their polarity while flash extent density adds a value of 1 to a grid column every time it contains at least one positive or negative point from a lightning flash.

Of particular interest is the evolution of the simulated eyewall lightning asymmetries, as they are associated with asymmetries in the eyewall convection. For example, the storm exhibits a dominant wavenumber-2 mode of both lightning metrics at 2200 UTC 28 August (Figs. 8a,c) and a dominant wavenumber-1 mode at

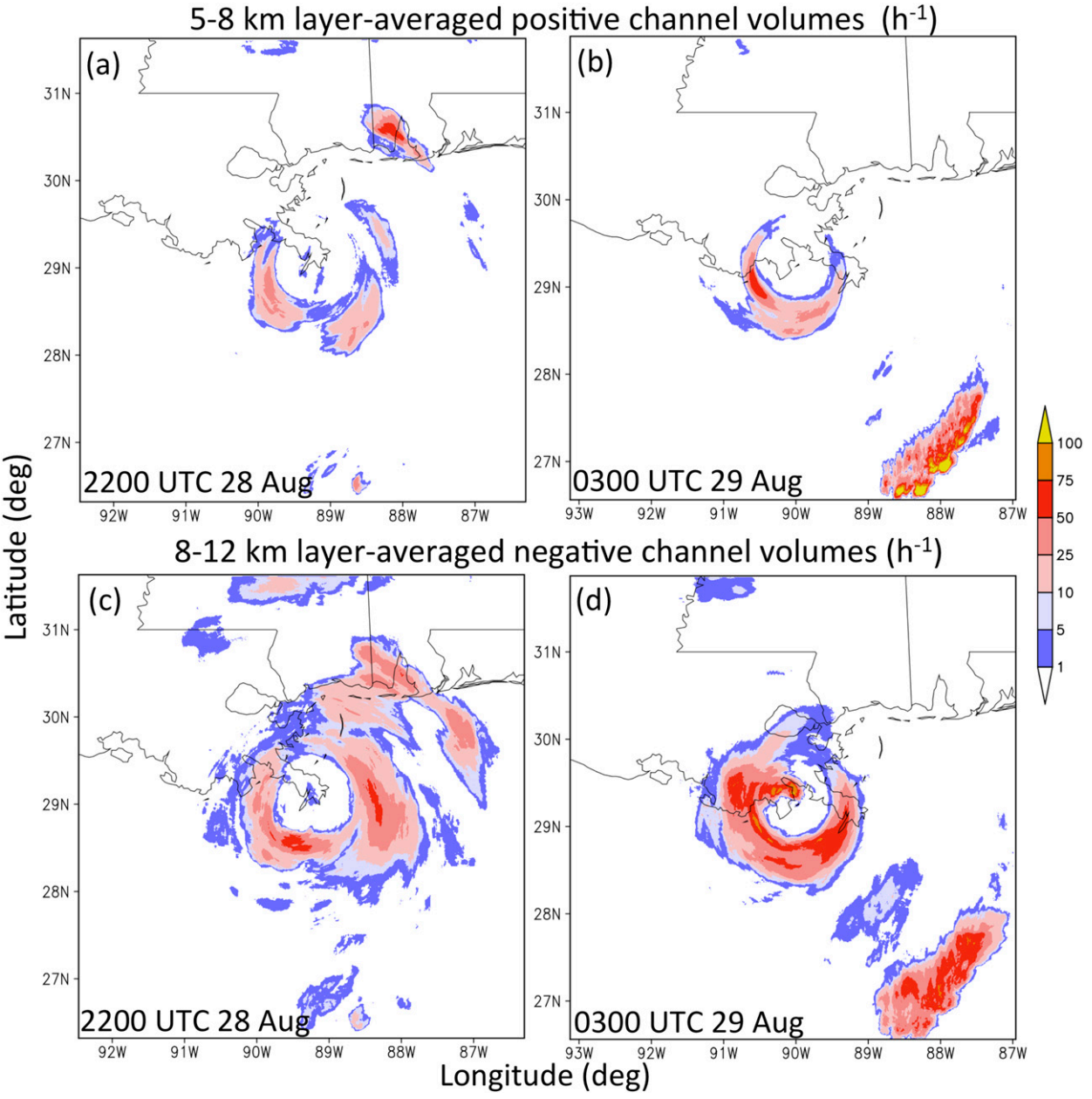

FIG. 9. As in Fig. 8, but for the positive channel volumes (h^{-1}) averaged over the z = 5–8-km layer at (a) 0000 and (b) 0300 UTC 29 Aug. (c),(d) As in (a),(b), but for the negative channel volumes (h^{-1}) averaged over the z = 8–12-km layer.

0300 UTC 29 August (Figs. 8b,d). Given a simulated storm track generally to the northwest (Fig. 1) in an environment characterized by weak midtropospheric southwesterly shear [~(3–4) m s^{-1}; not shown], the lightning maxima are expected to be collocated with maximum vertical velocities in the eyewall, which are generally located to the left of the track (e.g., Black et al. 2002; Chen et al. 2006; Shapiro 1983; Shapiro and Franklin 1999; Corbosiero and Molinari 2002, 2003). Because the vertical velocity field is instantaneous while the LCVs are accumulated over an hour, Fig. 8 is unable to show consistently this relationship between lightning and updrafts. However, initial test simulations with coarser grids and more frequent output (not shown) did show that lightning maxima typically were near updraft maxima to the left of the track.

The bulk of the channel volumes extending radially outward are of negative polarity and generally are located at higher levels than the positive channel volumes (Figs. 9 and 10c). The vertical arrangement of channel

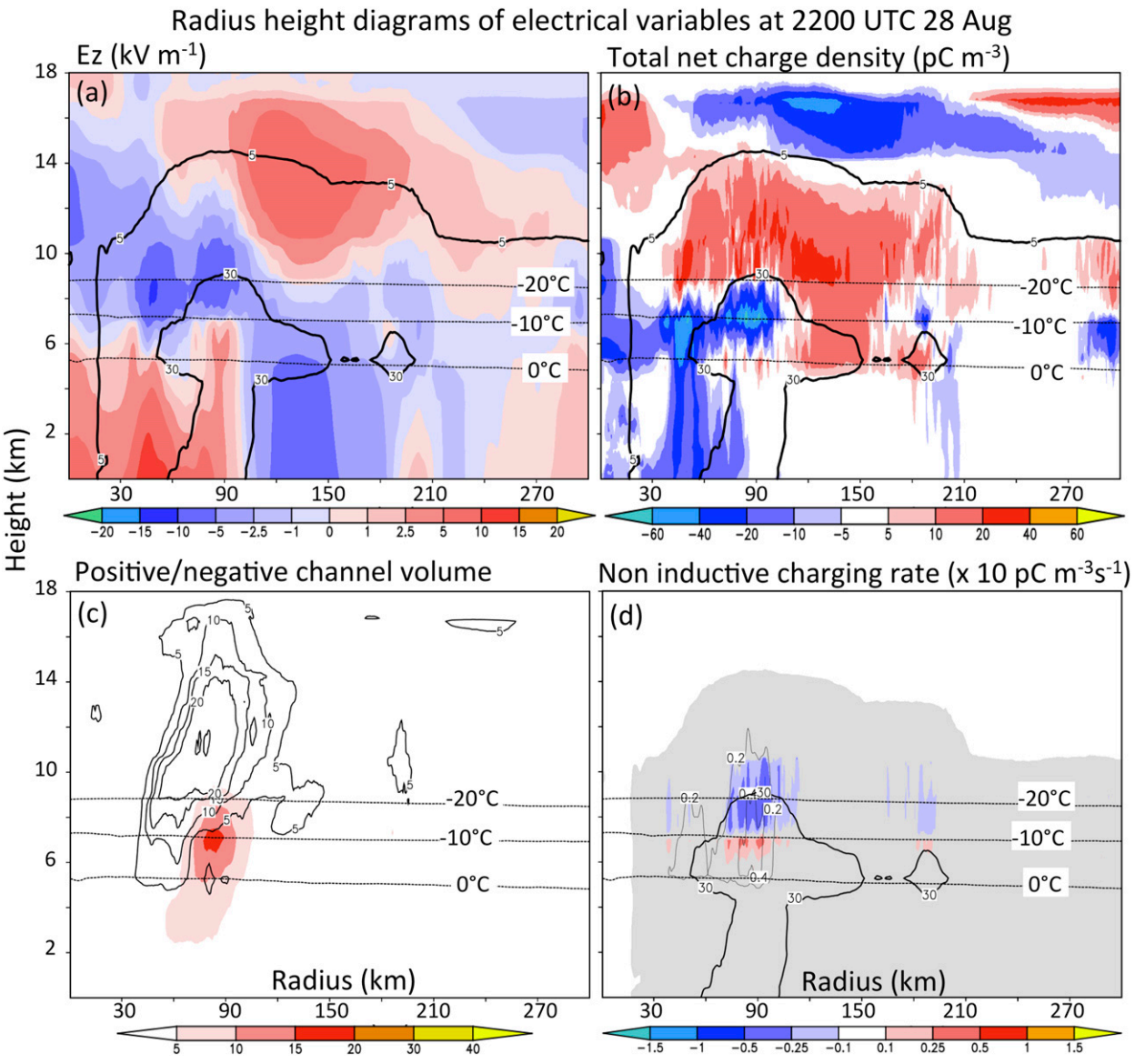

FIG. 10. As in Fig. 6, but for selected simulated electrical variables at 2200 UTC 28 Aug. (a) The vertical component of the ambient electric field (kV m^{-1}) in color shading overlain with the 5- and 30-dBZ contours (solid black lines). (b) As in (a), but for the total net charge density (pC m^{-3}). (c) Positive (shaded) and negative (thin black line) channel volumes. (d) Noninductive charging rates (10 pC m^{-3} s^{-1}) overlain with the 5-dBZ (gray shading) and 30-dBZ contours (solid black line) and graupel mixing ratio by increments of 0.2 g kg^{-1} (thin solid contours). For reference, all panels show the azimuthally averaged 0°, −10°, and −20°C isotherms, which are representative of the electrically active, mixed-phase region.

volume polarities (Figs. 9 and 10c) arises from the existence of a main midlevel negative charge layer between z = 5 and 8.5 km and a relatively deep positive charge layer above it between z = 8.5 and 15 km (Fig. 10b). The gross charge structure resembles a normal tripole in the range interval R = 70–100 km, as indicated by a main negative charge region between two main regions of positive charge (Williams 1989; Black and Hallett 1999). Radially inward between R = 40 and 70 km, the axisymmetric charge structure transitions to a normal dipole defined as a positive charge region atop negative charge. Sedimentation of snow particles outside the eyewall region (i.e., R > 100 km) results in the upper positive charge region extending downward to about z = 5 km (Fig. 10b). In response to the large volume of positive charge in the anvil (Fig. 10b), a prominent negative screening charge layer forms at cloud top between z = 15 and 18 km above the positive charge. As this negative screening layer charge sediments to lower altitudes radially outward (R > 200 km)

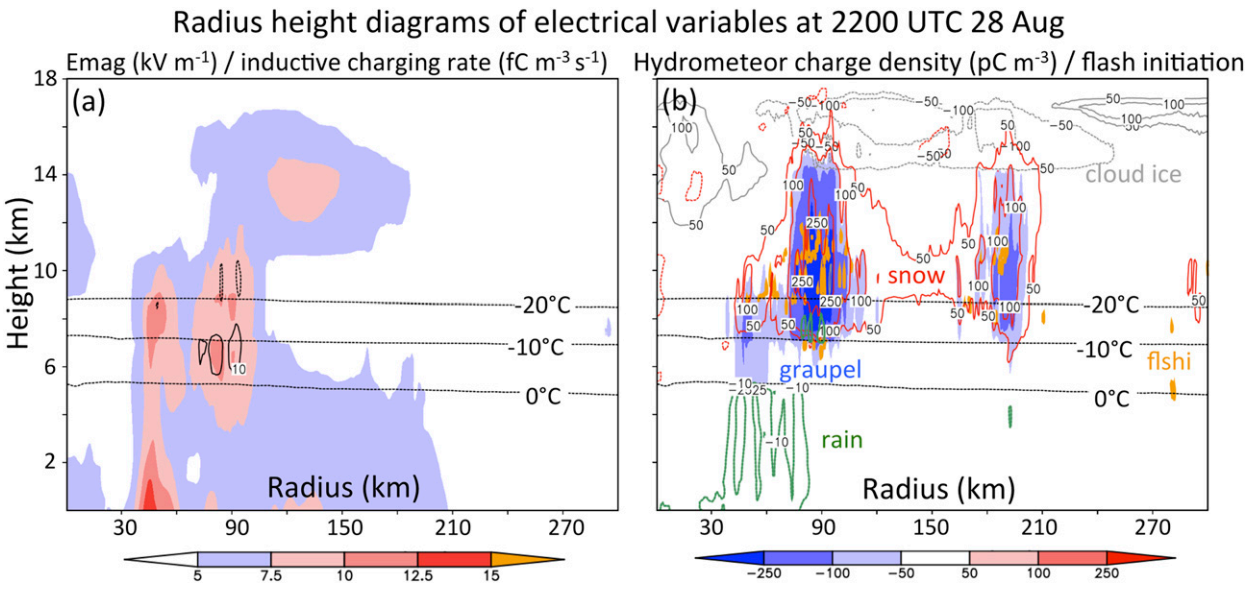

FIG. 11. As in Fig. 10, but for (a) the electric field magnitude (shaded, kV m^{-1}) overlain with the inductive charging rate (fC m^{-3} s^{-1}) and (b) the charge density (pC m^{-3}) on rain (green), snow (red), cloud ice (gray dashed line), and graupel (blue shading) overlain with flash initiation locations (contour of 1) in orange shading. For convenience, the color coding of each of the hydrometeor species in (b) also is indicated by text in their corresponding color.

between $z = 12$ and 15 km, a new positive screening layer charge forms above it (Fig. 10b). Similar vertical arrangement of screening layers of alternate polarity of charge have been documented within large stratiform anvils associated with deep continental convective storms (e.g., Byrne et al. 1989; ZM94; Weiss et al. 2012).

Two main persistent regions of the simulated maximum vertical component of the electric field E_z (i.e., E_{mag}) are situated between $R = 30$ and 90 km centered near $z = 8$ km and between $R = 90$ and 150 km centered near $z = 13.5$ km (Figs. 10a and 11a). The first region of maximum E_{mag} (associated with negative E_z) arises from the main midlevel negative charge region and the upper positive charge region in the eyewall. The second E_{mag} maximum aloft (associated with positive E_z) is attributed to the upper main positive charge region and the overlying negative charge screening layer. The regions of largest inductive and noninductive charging magnitudes are collocated with the main midlevel negative charge region in the eyewall, namely between $R = 30$ and 90 km at elevations ranging from $z = 6$ to 10 km (Figs. 10a and 11a). These altitudes of maximum charging rates appear higher than those suggested in the conceptual model of Black and Hallett (1999). Inductive charging rates in this simulation generally are about two orders of magnitude smaller than noninductive charging rates (Figs. 10a and 11a) owing to low droplet concentrations relative to those found within continental storms (not shown). Thus, in this simulation the main midlevel negative charge region in the mixed-phase region in the eyewall is attributed to negative noninductive charging of graupel (Figs. 10b,d and Fig. 11b) with minimal contribution from inductive charging (Fig. 11a). As the lighter snow particles collide with graupel, they are left with an excess positive charge as they ascend into the anvil (Figs. 10b,d and 11b). The negative charge below the melting level is associated with the melting of the negatively charged graupel into rain (Figs. 10b and 11b). The relatively smaller pockets of positive charge beneath the main negative charge near the freezing level in the eyewall ($R = 60$–100 km) arise from graupel acquiring positive charge at higher temperatures and larger liquid water contents (Saunders and Peck 1998; Black and Hallett 1999). The screening charge is carried by ice crystals near cloud top (Figs. 10b and 11b).

Time–height diagrams of net space charge volumes (+0.5 and −0.5 nC m^{-3} thresholds) in the eyewall illustrate both the dominance and persistence of a normal tripole gross charge structure (Fig. 12a). In this simulation, lightning flashes chiefly originated in three distinct layers, with most initiating between $z = 10$ and 12 km followed by a secondary maxima between about $z = 7$ and 7.5 km (Figs. 11b and 12b) with the remainder initiating near $z = 9$ km. The lowest region of flash initiation near 7 km is associated with the interface between the lower positive charge region and the main midlevel negative charge region on graupel in the eyewall region near $R = 60$–100 km (Figs. 12a,b and 10b).

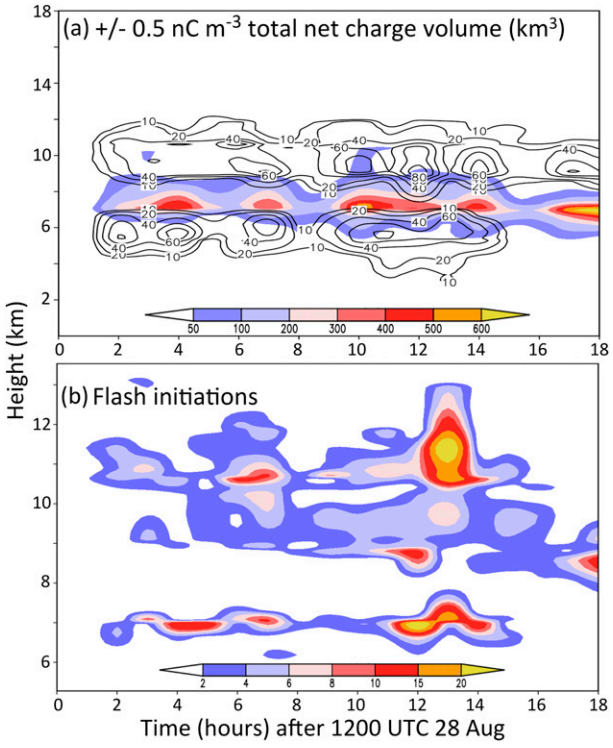

FIG. 12. Time–height diagram of (a) volume of total net charge density $> 0.5\,\text{nC m}^{-3}$ (solid black contours) and volume of total net charge density $< -0.5\,\text{nC m}^{-3}$ (shaded) for the eyewall region (cylinder of radius $R = 100$ km). The volumes for a given variable A interpolated on the cylindrical grid are computed as follows: At each level in the model, an algorithm loops through all the points within that level and counts instances when A exceeds a predetermined, fixed threshold. Once the total count is determined at this level, the latter is multiplied by the averaged volume of the grid cell. An average volume is employed, because the gridcell volumes at lower levels are penalized relative to those at upper levels as a result of the stretched vertical grid. In this simulation, the domain-averaged vertical grid spacing over the ocean where the eyewall evolves is ~370 m. (b) Time–height diagram of total flash initiations for the eyewall region. Note that in (b), the scale on the vertical axis is zoomed over the ~6–13-km layer to better discern the contours.

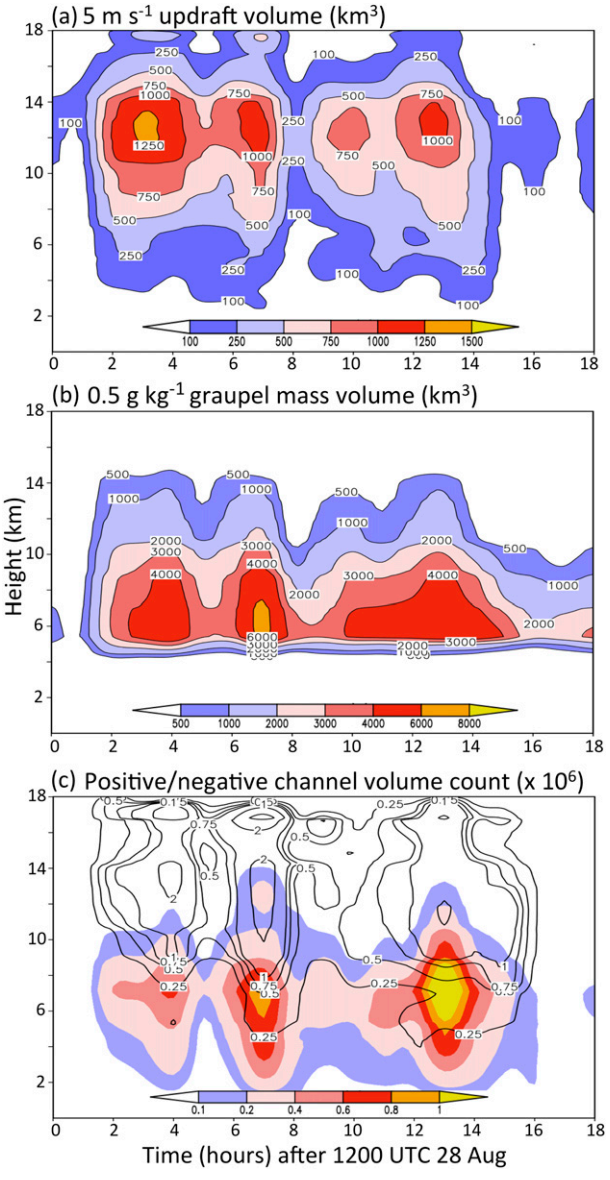

FIG. 13. As in Fig. 12, but for (a) the $5\,\text{m s}^{-1}$ updraft volume (km^3) and (b) $0.5\,\text{g kg}^{-1}$ graupel mass (km^3). (c) Total sum of positive (shading) and negative (solid black contours) channel volumes ($\times 10^6$). All the volumes were computed for the eyewall region delineated by a storm-centered cylinder of radius $R = 100$ km.

The upper flash initiation region centered near about $z = 9$ km is associated with the interface between the main midlevel negative charge region and the main upper positive charge region, both of which are persistent features in time and space in the eyewall (Figs. 10b, 11b, and 12a,b). Further analysis revealed that the peaks in flash initiation near or above 10.5 km at hours 7 and 13 arise from the existence of deeper, longer-lived (~1 h) convective towers in the eyewall (as hinted in Fig. 13a). As charged particles are being lofted in these strong deep convective updrafts (e.g., MacGorman et al. 1989; Fierro et al. 2006), the interface between the main midlevel charge region and the main upper positive charge region locates at higher altitudes [~(10–12) km]. The probability of flash initiation also increases with height for a given electric field magnitude, owing to the inverse exponential relationship of the breakdown field with height (e.g., Dwyer 2003).

c. *Relationships between lightning, microphysics, and kinematics*

Consistent with past modeling (e.g., Mansell et al. 2005; Fierro et al. 2006; Kuhlman et al. 2006) and

observational studies within deep continental storms (Wiens et al. 2005), the time–height evolution of positive and negative LCVs in the eyewall (Fig. 13c) is coincident in time with the eyewall graupel volume (Fig. 13b, threshold of 0.5 g kg^{-1}) and the 5 m s^{-1} updraft volume (Fig. 13a): the relative peaks in eyewall LCVs at hours 7 and 13 (Fig. 13c) are coincident with relative peaks in eyewall flash rates, in both instances marking the end of an intensification phase (Fig. 2b), which is consistent with the findings of DeMaria et al. (2012). In line with Fierro and Reisner (2011), the end of both intensification phases are coincident with a relative increase in eyewall updraft volume (Figs. 2b and 13a) and a relative increase in eyewall graupel volume (Figs. 2b and 13b).

Following a methodology similar to Fierro and Reisner (2011) that infuses seminal observational analysis methods of Petersen et al. (2005), a series of contour histograms were computed for the eyewall region that relate LCV to several variables known to be well associated with lightning (Fig. 14). Because all lightning metrics (Figs. 2 and 8) are time-integrated fields, the simulation was repeated using a finer temporal output frequency on D02 (i.e., 5 min versus 1 h) to better capture the kinematic and microphysical states associated with the occurrence of lightning in the model. Because of the high computational cost of this problem, the simulation was only advanced up to 1400 UTC 28 August (i.e., 2 h on D02), with the analysis focusing on the 1-h period following the electrification spinup between 1300 and 1400 UTC 28 August (Fig. 2b). Because lightning is strongly tied to the presence of riming ice and ice crystals (noninductive charging), we expect the results obtained during this earlier period to remain representative of the entire simulation.

The high-temporal-resolution simulation produces total ice water path (IWP) and IWP-P05, as defined in Petersen et al. (2005), that increase nearly linearly with 5-min LCV rates (Figs. 14b,c). A similar linear relationship is seen for composite reflectivity at temperatures less than −10°C, the graupel + hail path, and the ice + snow path (Figs. 14d–f). There appears to be an asymptotic, nonlinear association between LWP and LCV, with relatively high counts at either low LWP or low LCV (Fig. 14a). Similar to Petersen et al. (2005), bootstrapped correlations between LCV rates and the mean value of these variables were computed (Fig. 15). Since the mean value does not account for the spread in the data (Fig. 14), these correlations were recalculated using the raw model data as well (yielding $\sim 10^6$ pairs for each variable) and also are shown in Fig. 15. Accounting for the spread has the primary effect of reducing the most significant correlations (Fig. 15). Both IWP metrics exhibited the highest overall correlations with r values generally exceeding 0.7 followed by the graupel + hail path ($r \sim 0.7$), composite reflectivity at temperatures less than −10°C and the snow + ice path ($r \sim 0.5$) with the lowest being LWP ($r \sim 0.3$).

6. Conclusions

A high-resolution (350-m grid spacing) simulation of the electrification and lightning within a tropical cyclone was analyzed together with available total lightning observations to gain a better understanding of the small-scale electrification processes within these systems. The general environment and trends of Hurricane Isaac (2012), whose lightning activity was observed by the Earth Networks Total Lightning Network, were utilized to produce a reasonable tropical cyclone simulation. The numerical model in this work employs explicit electrification and lightning parameterizations implemented within the Weather Research and Forecasting Model (Fierro et al. 2013).

Overall, the simulated flash density rates remained comparable to those detected by the Earth Networks. In contrast to the observations, however, most of the simulated lightning occurred within the eyewall rather than the outer rainbands. These differences in lightning behavior were traced to disparities in basic structural traits of the convection within these two regions of the storm. Notably, the simulation produced larger axisymmetric reflectivities and deeper convection in the eyewall than is typically observed, which is a longstanding issue in cloud-resolving models (e.g., Rogers et al. 2007; Davis et al. 2010). Vertical frequency diagrams of radar reflectivity and the projection of the radar reflectivity fields onto the axisymmetric mode through azimuthal averaging confirmed this result and helped to quantify these differences.

The deep convective cells in some regions of the eyewall were either characterized by a normal tripole charge structure (similar to Fierro et al. 2007; Fierro and Reisner 2011) or by a positive dipole. This dipole exhibited a deep lower negative charge region extending down to the surface. The main negative charge layer at middle levels largely was attributed to negative noninductive charging of graupel, leaving in turn an excess positive charge on the lighter snow particles as they ascended into a radially extensive, deep anvil cloud (e.g., Marks and Houze 1987). As this graupel melted into rain and fell to lower levels, it extended the lower negative charge region down to the surface. The lowest positive charge region of the tripole was associated with positive noninductive charging of graupel at greater ambient temperatures and higher liquid water contents. A

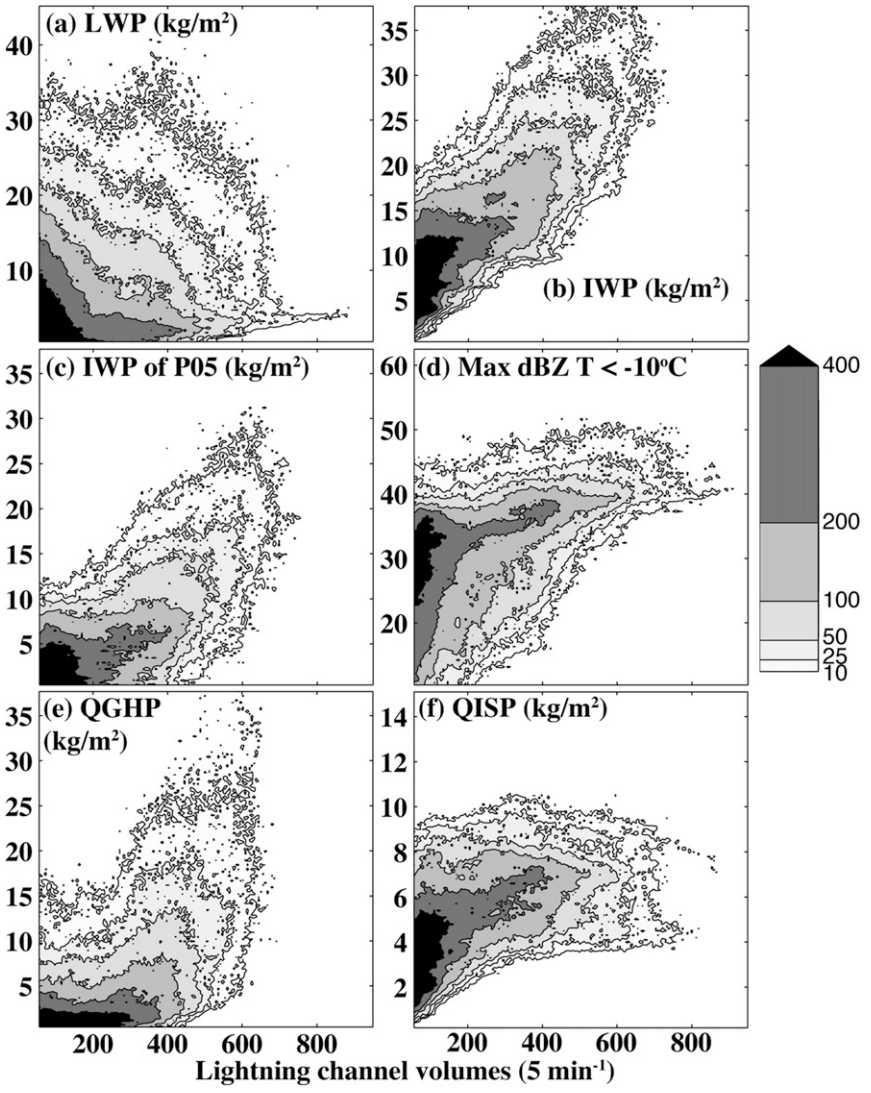

FIG. 14. Contour plot histograms between 5-min accumulated LCV in the model for the eyewall region with the following quantities: (a) liquid water path (LWP; kg m^{-2}); (b) total ice water path (IWP; kg m^{-2}); (c) as in (b), but for IWP in the layer between the −10°C isotherm and an assumed echo-top reflectivity threshold set at 20 dBZ [similar to Petersen et al. (2005)]; (d) composite reflectivity (dBZ) at ambient temperatures < −10°C; (e) graupel + hail path (QGHP; kg m^{-2}); and (f) ice + snow path (QISP, kg m^{-2}). The IWP in (b) does account for all ice species (namely, cloud ice, snow, hail, and graupel), while in (c) cloud ice was not accounted for because these are not properly detected by precipitation radars. To avoid rounding errors incurred by interpolating the data onto a cylindrical grid, the histograms were constructed using the data on the native Cartesian grid with the eyewall region defined by a storm-centered 200 × 200 km^2 square. All the variables on the x and y axes were partitioned into 150 equally sized bins. To establish more meaningful relationships between accumulated lightning fields and instantaneous microphysical and kinematical fields, the simulation was repeated for the first 2 h on the inner nest using a 5-min output frequency. The histograms cover the period between 1300 and 1400 UTC 28 Aug—namely, after the initial spinup incurred by activating the electrification when the inner nest is spawned at 1200 UTC 28 Aug (see Fig. 2b). To focus on the electrically active regions, the binning interval for LCV started at 50 by increments of 6.

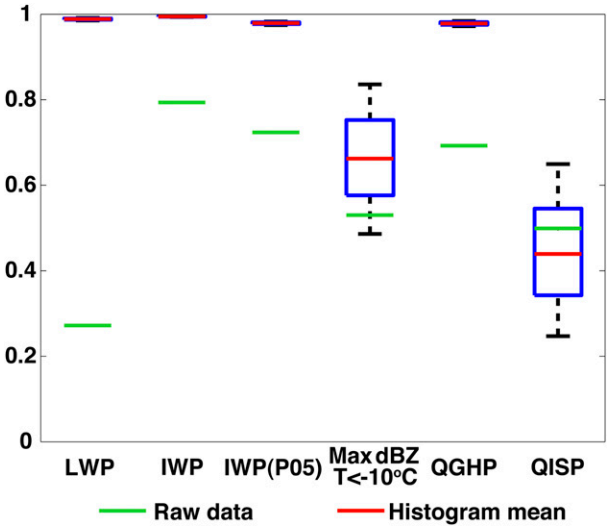

FIG. 15. Box-and-whisker plots of 1000-sample bootstrapped Pearson's correlation between the 5-min accumulated LCV and the six variables of Fig. 14 (shown on the x axis in the same order for convenience). The variables are partitioned into 150 equally sized bins in the eyewall region between 1300 and 1400 UTC 28 Aug. The red line depicts the median correlation. The blue box shows the lower and upper quartile (25% and 75%). The 2.5- and 97.5-percentile correlation values are shown at the end bars of the dotted lines outside the blue box. To compute the correlations, the mean value of the variable first was determined at each of the 150 LCV bin. Bootstrapping was applied on these correlations owing to the relatively small sample size. Because the averaging does not take into account the data spread, the correlations were computed again (shown in green) using the raw model data as follows: wherever LCV exceeded an assumed minimum of 50, the values of LCV and each of the six variables shown on the x axis were stored yielding a dataset comprising ~1 million pairs for each variable. Because of this large sample size, bootstrapping was not employed. For IWP, the linear regression line is given by IWP = 0.02 LCV + 2.52.

persistent, strong negative screening layer developed on the lighter ice crystals near cloud top in response to a deep, radially extensive volume of positively charged snow particles at upper levels.

Consistent with past modeling and observational studies on continental convection, lightning rates exhibited a good association with $5\,\mathrm{m\,s^{-1}}$ updraft volume and $0.5\,\mathrm{g\,kg^{-1}}$ graupel mass volume. The total lightning/electrical activity also was found to be well correlated with icewater path and graupel + hail path ($r > 0.7$) and moderately correlated with composite reflectivity at ambient temperatures less than −10°C and the snow + ice path ($r \sim 0.5$). In line with DeMaria et al. (2012), relative maxima in eyewall lightning rates were coincident with the end of an intensification phase.

Because some of the aforementioned proxy variables are readily observed or derived from various remote sensing platforms and instruments (e.g., radar, satellites), such statistics/linear relationships could be useful toward developing functional relationships to assimilate lightning data into numerical weather prediction models. Further case studies could also help establish possible use of continuous total lightning monitoring (e.g., by GLM) for diagnosis of TC intensity changes.

The upcoming launch of the GOES-R GLM in the forthcoming years will provide a unique opportunity to augment our understanding of the relationships between total lightning and intensity changes within TCs. The remote sensing instruments utilized to study the lightning produced by TCs until now have detected mainly CG flashes within TCs—especially far out to sea. When total lighting observations become available, it would be relevant to determine whether the relationships between intensity changes and lightning bursts documented in observations so far continue to hold—either in the eyewall or the outer bands. More specifically, could intracloud flash bursts alone serve as a more systematic surrogate for imminent intensity change (Fierro et al. 2011)? If yes, are there preferred regions along the track of sheared/unsheared storms where such bursts would show a high correlation with intensity changes and, if yes, what would be the average lead time?

Motivation for this research is rooted in observational works focusing on continental storms, which showed that an increase in CG flash rates typically was correlated with the descent of reflectivity cores and updraft weakening while an increase in IC flash rate was correlated with updraft intensification and the lofting of charged ice particles (e.g., MacGorman and Rust 1998; Wiens et al. 2005; Schultz et al. 2011). If a similar behavior occurs in TC eyewalls, it may explain why a CG flash burst in the eyewall can occur near the end of an intensification phase (DeMaria et al. 2012). Also, because the results herein are derived from a single model realization that is based on the initial and boundary conditions of one particular case, studies of additional cases are needed to further test and, potentially, generalize some of the results reported in this work.

Acknowledgments. The authors thank Bill Callahan, Benny Chukrun, Stan Heckman, Christopher Sloop, and Jim Anderson from Earth Networks for providing the total lightning data and Carrie Langston for providing the NSSL NMQ data. Funding was provided by NOAA/Office of Oceanic and Atmospheric Research under NOAA–University of Oklahoma Cooperative Agreement NA11OAR4320072, U.S. Department of Commerce. This work was further supported by the National Oceanic and Atmospheric Administration (NOAA) of the U.S. Department of Commerce under Grant

NOAA-OAR-CIPO-2014-2003893. The computationally intensive simulation analyzed in this manuscript was made possible through research allocations obtained on the high-performance cluster (HPC) "Stampede" hosted by the Texas Advances Computing Center (TACC) under Grants ATM140027 and ATM140032. Code development, optimization, and testing made use of computing resources provided by NOAA (HPC "Jet"). Auxiliary computing resources were also provided by the Oklahoma Supercomputing Center for Education and Research (OSCER) hosted at the University of Oklahoma. The authors also are grateful to two anonymous reviewers, John Knaff and Jack Kain, for providing helpful suggestions on an earlier version of the manuscript. Thanks also go out to John Cazes from TACC for providing valuable technical support.

REFERENCES

Abarca, S. F., K. L. Corbosiero, and D. Vollaro, 2011: The World Wide Lightning Location Network and convective activity in tropical cyclones. *Mon. Wea. Rev.*, **139**, 175–191, doi:10.1175/2010MWR3383.1.

Aksoy, A., D. C. Dowell, and C. Snyder, 2009: A multicase comparative assessment of the ensemble Kalman filter for assimilation of radar observations. Part I: Storm-scale analyses. *Mon. Wea. Rev.*, **137**, 1805–1824, doi:10.1175/2008MWR2691.1.

Anthes, R. A., 2003: Hot towers and hurricanes: Early observations, theories, and models. *Cloud Systems, Hurricanes, and the Tropical Rainfall Measuring Mission (TRMM), Meteor. Monogr.*, No. 51, Amer. Meteor. Soc., 139–148, doi:10.1175/0065-9401(2003)029<0139:CHTAHE>2.0.CO;2.

Avila, E. E., G. M. Caranti, N. E. Castellano, and C. P. R. Saunders, 1998: Laboratory studies of the influence of cloud droplet size on charge transfer during crystal-graupel collisions. *J. Geophys. Res.*, **103**, 8985–8996, doi:10.1029/97JD03115.

Black, M. L., R. W. Burpee, and F. D. Marks, 1996: Vertical motion characteristics of tropical cyclones determined with airborne Doppler radial velocities. *J. Atmos. Sci.*, **53**, 1887–1909, doi:10.1175/1520-0469(1996)053<1887:VMCOTC>2.0.CO;2.

——, J. F. Gamache, F. D. Marks Jr., C. E. Samsury, and H. E. Willoughby, 2002: Eastern Pacific Hurricanes Jimena of 1991 and Olivia of 1994: The effect of vertical shear on structure and intensity. *Mon. Wea. Rev.*, **130**, 2291–2312, doi:10.1175/1520-0493(2002)130<2291:EPHJOA>2.0.CO;2.

Black, R. A., and J. Hallett, 1999: Electrification of the hurricane. *J. Atmos. Sci.*, **56**, 2004–2028, doi:10.1175/1520-0469(1999)056<2004:EOTH>2.0.CO;2.

Boccippio, D. J., K. L. Cummins, H. J. Christian, and S. J. Goodman, 2001: Combined satellite- and surface-based estimation of the intracloud-cloud-to-ground lightning ratio over the continental United States. *Mon. Wea. Rev.*, **129**, 108–122, doi:10.1175/1520-0493(2001)129<0108:CSASBE>2.0.CO;2.

Bovalo, C., C. Barthe, N. Yu, and N. Bègue, 2014: Lightning activity within tropical cyclones in the South West Indian Ocean. *J. Geophys. Res. Atmos.*, **119**, 8231–8244, doi:10.1002/2014JD021651.

Brooks, I. M., C. P. R. Saunders, R. P. Mitzeva, and S. L. Peck, 1997: The effect on thunderstorm charging of the rate of rime accretion by graupel. *Atmos. Res.*, **43**, 277–295, doi:10.1016/S0169-8095(96)00043-9.

Bryan, G. H., J. C. Wyngaard, and J. M. Fritsch, 2003: Resolution requirements for the simulation of deep moist convection. *Mon. Wea. Rev.*, **131**, 2394–2416, doi:10.1175/1520-0493(2003)131<2394:RRFTSO>2.0.CO;2.

Byrne, G. J., A. A. Few, and M. F. Stewart, 1989: Electric field measurements within a severe thunderstorm anvil. *J. Geophys. Res.*, **94**, 6297–6307, doi:10.1029/JD094iD05p06297.

Calhoun, K. M., E. R. Mansell, D. R. MacGorman, and D. C. Dowell, 2014: Numerical simulations of lightning and storm charge of the 29–30 May 2004 Geary, Oklahoma, supercell thunderstorm using EnKF mobile radar data assimilation. *Mon. Wea. Rev.*, **142**, 3977–3997, doi:10.1175/MWR-D-13-00403.1.

Cecil, D. J., and E. J. Zipser, 2002: Reflectivity, ice scattering, and lightning characteristics of hurricane eyewalls and rainbands. Part II: Intercomparison of observations. *Mon. Wea. Rev.*, **130**, 785–801, doi:10.1175/1520-0493(2002)130<0785:RISALC>2.0.CO;2.

——, ——, and S. W. Nesbitt, 2002: Reflectivity, ice scattering, and lightning characteristics of hurricane eyewalls and rainbands. Part I: Quantitative description. *Mon. Wea. Rev.*, **130**, 769–784, doi:10.1175/1520-0493(2002)130<0769:RISALC>2.0.CO;2.

Chen, F., and J. Dudhia, 2001: Coupling an advanced land surface–hydrology model with the Penn State–NCAR MM5 modeling system. Part I: Model implementation and sensitivity. *Mon. Wea. Rev.*, **129**, 569–585, doi:10.1175/1520-0493(2001)129<0569:CAALSH>2.0.CO;2.

——, Z. Janjić, and K. Mitchell, 1997: Impact of atmospheric surface-layer parameterizations in the new land-surface scheme of the NCEP mesoscale Eta model. *Bound.-Layer Meteor.*, **85**, 391–421, doi:10.1023/A:1000531001463.

Chen, S. S., J. A. Knaff, and F. D. Marks Jr., 2006: Effects of vertical wind shear and storm motion on tropical cyclone rainfall asymmetries deduced from TRMM. *Mon. Wea. Rev.*, **134**, 3190–3208, doi:10.1175/MWR3245.1.

Chiu, C.-S., 1978: Numerical study of cloud electrification in an axisymmetric time-dependent cloud model. *J. Geophys. Res.*, **83**, 5025–5049, doi:10.1029/JC083iC10p05025.

Coleman, L. M., T. C. Marshall, M. Stolzenburg, T. Hamlin, P. R. Krehbiel, W. Rison, and R. J. Thomas, 2003: Effects of charge and electrostatic potential on lightning propagation. *J. Geophys. Res.*, **108**, 4298, doi:10.1029/2002JD002718.

Corbosiero, K. L., and J. Molinari, 2002: The effects of vertical wind shear on the distribution of convection in tropical cyclones. *Mon. Wea. Rev.*, **130**, 2110–2123, doi:10.1175/1520-0493(2002)130<2110:TEOVWS>2.0.CO;2.

——, and ——, 2003: The relationship between storm motion, vertical wind shear, and convective asymmetries in tropical cyclones. *J. Atmos. Sci.*, **60**, 366–376, doi:10.1175/1520-0469(2003)060<0366:TRBSMV>2.0.CO;2.

Davis, C., W. Wang, J. Dudhia, and R. Torn, 2010: Does increased horizontal resolution improve hurricane wind forecasts? *Wea. Forecasting*, **25**, 1826–1841, doi:10.1175/2010WAF2222423.1.

DeMaria, M., R. T. DeMaria, J. A. Knaff, and D. Molenar, 2012: Tropical cyclone lightning and rapid intensity change. *Mon. Wea. Rev.*, **140**, 1828–1842, doi:10.1175/MWR-D-11-00236.1.

——, C. R. Sampson, J. A. Knaff, and K. D. Musgrave, 2014: Is tropical cyclone intensity guidance improving? *Bull. Amer. Meteor. Soc.*, **95**, 387–398, doi:10.1175/BAMS-D-12-00240.1.

Didlake, A. C., Jr., and R. A. Houze Jr., 2013: Dynamics of the stratiform sector of a tropical cyclone rainband. *J. Atmos. Sci.*, **70**, 1891–1911, doi:10.1175/JAS-D-12-0245.1.

Dwyer, J. R., 2003: A fundamental limit on electric fields in air. *Geophys. Res. Lett.*, **30**, 2055, doi:10.1029/2003GL017781.

Ek, M. B., K. E. Mitchell, Y. Lin, E. Rogers, P. Grunmann, V. Koren, G. Gayno, and J. D. Tarpley, 2003: Implementation of Noah land surface model advances in the National Centers for Environmental Prediction operational mesoscale Eta model. *J. Geophys. Res.*, **108**, 8851, doi:10.1029/2002JD003296.

Emersic, C., and C. P. R. Saunders, 2010: Further laboratory investigations into the relative diffusional growth rate theory of thunderstorm electrification. *Atmos. Res.*, **98**, 327–340, doi:10.1016/j.atmosres.2010.07.011.

Fierro, A. O., and J. M. Reisner, 2011: High-resolution simulation of the electrification and lightning of Hurricane Rita during the period of rapid intensification. *J. Atmos. Sci.*, **68**, 477–494, doi:10.1175/2010JAS3659.1.

——, M. S. Gilmore, E. R. Mansell, L. J. Wicker, and J. M. Straka, 2006: Electrification and lightning in an idealized boundary-crossing supercell simulation of 2 June 1995. *Mon. Wea. Rev.*, **134**, 3149–3172, doi:10.1175/MWR3231.1.

——, L. M. Leslie, E. R. Mansell, J. M. Straka, D. R. MacGorman, and C. Ziegler, 2007: A high resolution simulation of the microphysics and electrification in an idealized hurricane-like vortex. *Meteor. Atmos. Phys.*, **98**, 13–33, doi:10.1007/s00703-006-0237-0.

——, ——, ——, and ——, 2008: Numerical simulations of the electrification and microphysics of the weakly electrified 9th February 1993 TOGA COARE squall line: Comparisons with observations. *Mon. Wea. Rev.*, **136**, 364–379, doi:10.1175/2007MWR2156.1.

——, R. F. Rogers, F. D. Marks, and D. S. Nolan, 2009a: The Impact of horizontal grid spacing on the microphysical and kinematic structures of strong tropical cyclones simulated with the WRF-ARW model. *Mon. Wea. Rev.*, **137**, 3717–3743, doi:10.1175/2009MWR2946.1.

——, J. Simpson, M. A. LeMone, J. M. Straka, and B. F. Smull, 2009b: On how hot towers fuel the Hadley cell: An observational and modeling study of line-organized convection in the equatorial trough from TOGA COARE. *J. Atmos. Sci.*, **66**, 2730–2746, doi:10.1175/2009JAS3017.1.

——, X.-M. Shao, J. M. Reisner, J. D. Harlin, and T. Hamlin, 2011: Evolution of eyewall convective events as indicated by intracloud and cloud-to-ground lightning activity during the rapid intensification of Hurricanes Rita and Katrina. *Mon. Wea. Rev.*, **139**, 1492–1504, doi:10.1175/2010MWR3532.1.

——, E. R. Mansell, C. Ziegler, and D. R. MacGorman, 2012: Application of a lightning data assimilation technique in the WRF-ARW model at cloud-resolving scales for the tornado outbreak of 24 May 2011. *Mon. Wea. Rev.*, **140**, 2609–2627, doi:10.1175/MWR-D-11-00299.1.

——, ——, ——, and ——, 2013: The implementation of an explicit charging and discharge lightning scheme within the WRF-ARW model: Benchmark simulations with a continental squall line and a tropical cyclone. *Mon. Wea. Rev.*, **141**, 2390–2415, doi:10.1175/MWR-D-12-00278.1.

——, J. Gao, C. Ziegler, E. R. Mansell, D. R. MacGorman, and S. Dembek, 2014: Evaluation of a cloud-scale lightning data assimilation technique and a 3DVAR method for the analysis and short-term forecast of the 29 June 2012 derecho event. *Mon. Wea. Rev.*, **142**, 183–202, doi:10.1175/MWR-D-13-00142.1.

——, A. J. Clark, E. R. Mansell, D. R. MacGorman, S. Dembek, and C. Ziegler, 2015: Impact of storm-scale lightning data assimilation on WRF-ARW precipitation forecasts during the 2013 warm season over the contiguous United States. *Mon. Wea. Rev.*, **143**, 757–777, doi:10.1175/MWR-D-14-00183.1.

Gao, J., and Coauthors, 2013: A real-time weather-adaptive 3DVAR analysis system for severe weather detections and warnings. *Wea. Forecasting*, **28**, 727–745, doi:10.1175/WAF-D-12-00093.1.

Gardiner, B., D. Lamb, R. L. Pitter, J. Hallet, and C. P. R. Saunders, 1985: Measurements of initial potential gradient and particles charges in a Montana thunderstorm. *J. Geophys. Res.*, **90**, 6079–6086, doi:10.1029/JD090iD04p06079.

Gentry, M. S., and G. M. Lackmann, 2010: Sensitivity of simulated tropical cyclone structure and intensity to horizontal resolution. *Mon. Wea. Rev.*, **138**, 688–704, doi:10.1175/2009MWR2976.1.

Goodman, S. J., and Coauthors, 2013: The GOES-R Geostationary Lightning Mapper (GLM). *Atmos. Res.*, **125–126**, 34–49, doi:10.1016/j.atmosres.2013.01.006.

Guimond, S. R., G. M. Heymsfield, and F. J. Turk, 2010: Multiscale observations of Hurricane Dennis (2005): The effects of hot towers on rapid intensification. *J. Atmos. Sci.*, **67**, 633–654, doi:10.1175/2009JAS3119.1.

Gurka, J. J., T. A. Schmit, T. M. Renkevens, M. M. Gunshor, and J. Li, 2006: 2006 update on baseline instruments for GOES-R series. *Atmospheric and Environmental Remote Sensing Data Processing and Utilization II: Perspective on Calibration/Validation Initiatives and Strategies*, A. H. L. Huang and H. J. Bloom, Eds., International Society for Optical Engineering (SPIE Proceedings, Vol. 6301), 63010H, doi:10.1117/12.683701.

Helsdon, J. H., Jr., and R. D. Farley, 1987: A numerical modeling study of a Montana thunderstorm. Part II: Model results vs. observations involving the electrical aspects. *J. Geophys. Res.*, **92**, 5661–5675, doi:10.1029/JD092iD05p05661.

Hence, D. A., and R. A. Houze Jr., 2011: Vertical structure of hurricane eyewalls as seen by the TRMM Precipitation Radar. *J. Atmos. Sci.*, **68**, 1637–1652, doi:10.1175/2011JAS3578.1.

Hendricks, E. A., M. T. Montgomery, and C. A. Davis, 2004: The role of ''vortical'' hot towers in the formation of Tropical Cyclone Diana (1984). *J. Atmos. Sci.*, **61**, 1209–1232, doi:10.1175/1520-0469(2004)061<1209:TROVHT>2.0.CO;2.

——, M. S. Peng, X. Ge, and T. Li, 2011: Performance of a dynamic initialization scheme in the Coupled Ocean–Atmosphere Mesoscale Prediction System for Tropical Cyclones (COAMPS-TC). *Wea. Forecasting*, **26**, 650–663, doi:10.1175/WAF-D-10-05051.1.

Heymsfield, A. J., L. M. Miloshevich, C. Schmitt, A. Bansemer, C. Twohy, M. R. Poellot, A. Fridlind, and H. Gerber, 2005: Homogeneous ice nucleation in subtropical and tropical convection and its influence on cirrus anvil microphysics. *J. Atmos. Sci.*, **62**, 41–64, doi:10.1175/JAS-3360.1.

——, A. Bansemer, S. L. Durden, R. L. Herman, and T. Paul Bui, 2006: Ice microphysics observations in Hurricane Humberto: Comparison with non-hurricane-generated ice cloud layers. *J. Atmos. Sci.*, **63**, 288–308, doi:10.1175/JAS3603.1.

——, ——, G. Heymsfield, and A. O. Fierro, 2009: Microphysics of maritime tropical convective updrafts at temperatures from −20° to −60°. *J. Atmos. Sci.*, **66**, 3530–3562, doi:10.1175/2009JAS3107.1.

Houze, R. A., Jr., 2010: Clouds in tropical cyclones. *Mon. Wea. Rev.*, **138**, 293–344, doi:10.1175/2009MWR2989.1.

Janjić, Z. I., 1994: The step-mountain eta coordinate model: Further developments of the convection, viscous sublayer, and turbulence closure schemes. *Mon. Wea. Rev.*, **122**, 927–945, doi:10.1175/1520-0493(1994)122<0927:TSMECM>2.0.CO;2.

Jayaratne, E. R., C. P. R. Saunders, and J. Hallett, 1983: Laboratory studies of the charging of soft hail during ice crystal interactions. *Quart. J. Roy. Meteor. Soc.*, **109**, 609–630, doi:10.1002/qj.49710946111.

Jiang, G. S., and C. Shu, 1996: Efficient implementation of weighted ENO schemes. *J. Comput. Phys.*, **126**, 202–222, doi:10.1006/jcph.1996.0130.

Kaplan, J., and M. DeMaria, 2003: Large-scale characteristics of rapidly intensifying tropical cyclones in the North Atlantic basin. *Wea. Forecasting*, **18**, 1093–1108, doi:10.1175/1520-0434(2003)018<1093:LCORIT>2.0.CO;2.

——, ——, and J. A. Knaff, 2010: A revised tropical cyclone rapid intensification index for the Atlantic and eastern North Pacific basins. *Wea. Forecasting*, **25**, 220–241, doi:10.1175/2009WAF2222280.1.

Kelley, O. A., J. Stout, and J. B. Halverson, 2004: Tall precipitation cells in tropical cyclone eyewalls are associated with tropical cyclone intensification. *Geophys. Res. Lett.*, **31**, L24112, doi:10.1029/2004GL021616.

Khain, A., N. Cohen, B. Lynn, and A. Pokrovsky, 2008: Possible aerosol effects on lightning activity and structure of hurricanes. *J. Atmos. Sci.*, **65**, 3652–3677, doi:10.1175/2008JAS2678.1.

Kuhlman, K. M., C. L. Ziegler, E. R. Mansell, D. R. MacGorman, and J. M. Straka, 2006: Numerically simulated electrification and lightning of the 29 June 2000 STEPS supercell storm. *Mon. Wea. Rev.*, **134**, 2734–2757, doi:10.1175/MWR3217.1.

Landsea, C. W., and J. L. Franklin, 2013: Atlantic hurricane database uncertainty and presentation of a new database format. *Mon. Wea. Rev.*, **141**, 3576–3592, doi:10.1175/MWR-D-12-00254.1.

Lang, T. J., and S. A. Rutledge, 2002: Relationships between convective storm kinematics, precipitation, and lightning. *Mon. Wea. Rev.*, **130**, 2492–2506, doi:10.1175/1520-0493(2002)130<2492:RBCSKP>2.0.CO;2.

LeMone, M. A., and E. J. Zipser, 1980: Cumulonimbus vertical velocity events in GATE. Part I: Diameter, intensity, and mass flux. *J. Atmos. Sci.*, **37**, 2444–2457, doi:10.1175/1520-0469(1980)037<2444:CVVEIG>2.0.CO;2.

Liu, Y., D. L. Zhang, and M. K. Yau, 1997: A multiscale numerical study of Hurricane Andrew (1992). Part I: Explicit simulation and verification. *Mon. Wea. Rev.*, **125**, 3073–3093, doi:10.1175/1520-0493(1997)125<3073:AMNSOH>2.0.CO;2.

Lyons, W. A., M. G. Venne, P. G. Black, and R. C. Gentry, 1989: Hurricane lightning: A new diagnostic tool for tropical storm forecasting? Preprints, *18th Conf. on Hurricanes and Tropical Meteorology*, San Diego, CA, Amer. Meteor. Soc., 113–114.

MacGorman, D. R., and W. D. Rust, 1998: *The Electrical Nature of Storms*. Oxford University Press, 422 pp.

——, A. A. Few, and T. L. Teer, 1981: Layered lightning activity. *J. Geophys. Res.*, **86**, 9900–9910, doi:10.1029/JC086iC10p09900.

——, D. W. Burgess, V. Mazur, W. D. Rust, W. L. Taylor, and B. C. Johnson, 1989: Lightning rates relative to tornadic storm evolution on 22 May 1981. *J. Atmos. Sci.*, **46**, 221–251, doi:10.1175/1520-0469(1989)046<0221:LRRTTS>2.0.CO;2.

——, J. M. Straka, and C. L. Ziegler, 2001: A lightning parameterization for numerical cloud models. *J. Appl. Meteor.*, **40**, 459–478, doi:10.1175/1520-0450(2001)040<0459:ALPFNC>2.0.CO;2.

——, I. R. Apostolakopoulos, N. R. Lund, N. W. S. Demetriades, M. J. Murphy, and P. R. Krehbiel, 2011: The timing of cloud-to-ground lightning relative to total lightning activity. *Mon. Wea. Rev.*, **139**, 3871–3886, doi:10.1175/MWR-D-11-00047.1.

Mansell, E. R., 2014: Storm-scale ensemble Kalman filter assimilation of total lightning flash-extent data. *Mon. Wea. Rev.*, **142**, 3683–3695, doi:10.1175/MWR-D-14-00061.1.

——, and C. L. Ziegler, 2013: Aerosol effects on simulated storm electrification and precipitation in a two-moment bulk microphysics model. *J. Atmos. Sci.*, **70**, 2032–2050, doi:10.1175/JAS-D-12-0264.1.

——, D. R. MacGorman, C. L. Ziegler, and J. M. Straka, 2002: Simulated three-dimensional branched lightning in a numerical thunderstorm model. *J. Geophys. Res.*, **107**, doi:10.1029/2000JD000244.

——, ——, ——, and ——, 2005: Charge structure and lightning sensitivity in a simulated multicell storm. *J. Geophys. Res.*, **110**, D12101, doi:10.1029/2004JD005287.

——, C. L. Ziegler, and D. R. MacGorman, 2007: A lightning data assimilation technique for mesoscale forecast models. *Mon. Wea. Rev.*, **135**, 1732–1748, doi:10.1175/MWR3387.1.

——, ——, and C. Bruning, 2010: Simulated electrification of a small thunderstorm with two-moment bulk microphysics. *J. Atmos. Sci.*, **67**, 171–194, doi:10.1175/2009JAS2965.1.

Marchand, M. R., and H. E. Fuelberg, 2014: Assimilation of lightning data using a nudging method involving low-level warming. *Mon. Wea. Rev.*, **142**, 4850–4871, doi:10.1175/MWR-D-14-00076.1.

Marks, F. D., and R. A. Houze, 1987: Inner core structure of Hurricane Alicia from airborne Doppler radar observations. *J. Atmos. Sci.*, **44**, 1296–1317, doi:10.1175/1520-0469(1987)044<1296:ICSOHA>2.0.CO;2.

——, and L. K. Shay, 1998: Landfalling tropical cyclones: Forecast problems and associated research opportunities. *Bull. Amer. Meteor. Soc.*, **79**, 305–323, doi:10.1175/1520-0477(1998)079<0305:LTCFPA>2.0.CO;2.

Mellor, G. L., and T. Yamada, 1982: Development of turbulence closure model for geophysical fluid problems. *Rev. Geophys. Space Phys.*, **20**, 851–875, doi:10.1029/RG020i004p00851.

Michalakes, J., J. Dudhia, D. Gill, T. Henderson, J. Klemp, W. Skamarock, and W. Wang, 2005: The Weather Research and Forecast Model: Software architecture and performance. *Proc. 11th Workshop on High Performance Computing in Meteorology*, Reading, United Kingdom, ECMWF, 156–168.

Mlawer, E., S. Taubman, P. Brown, M. Iacono, and S. Clough, 1997: Radiative transfer for inhomogeneous atmospheres: RRTM, a validated correlated-k model for the longwave. *J. Geophys. Res.*, **102**, 16 663–16 682, doi:10.1029/97JD00237.

Molinari, J., P. K. Moore, V. P. Idone, R. W. Henderson, and A. B. Saljoughy, 1994: Cloud-to-ground lightning in Hurricane Andrew. *J. Geophys. Res.*, **99**, 16 665–16 676, doi:10.1029/94JD00722.

——, P. Moore, and V. Idone, 1999: Convective structure of hurricanes as revealed by lightning locations. *Mon. Wea. Rev.*, **127**, 520–534, doi:10.1175/1520-0493(1999)127<0520:CSOHAR>2.0.CO;2.

Montgomery, M. T., M. E. Nicholls, T. A. Cram, and A. B. Saunders, 2006: A vortical hot tower route to tropical cyclogenesis. *J. Atmos. Sci.*, **63**, 355–386, doi:10.1175/JAS3604.1.

Mossop, S. C., 1976: Production of secondary ice particles during the growth of graupel by riming. *Quart. J. Roy. Meteor. Soc.*, **102**, 45–57, doi:10.1002/qj.49710243104.

Nolan, D. S., Y. Moon, and D. P. Stern, 2007: Tropical cyclone intensification from asymmetric convection: Energetics and efficiency. *J. Atmos. Sci.*, **64**, 3377–3405, doi:10.1175/JAS3988.1.

Orville, R. E., and J. M. Coyne, 1999: Cloud-to-ground lightning in tropical cyclones (1986-1996). Preprints, *23rd Conf. on Hurricanes and Tropical Meteorology*, Dallas, TX, Amer. Meteor. Soc., 4A.12. [Available online at https://ams.confex.com/ams/older/99annual/abstracts/1695.htm.]

Pan, L., X. Qie, D. Liu, D. Wang, and J. Yang, 2010: The lightning activities in super typhoons over the Northwest Pacific. *Sci. China Earth Sci.*, **53**, 1241–1248, doi:10.1007/s11430-010-3034-z.

——, ——, and D. Wang, 2014: Lightning activity and its relation to the intensity of typhoons over the Northwest Pacific Ocean. *Adv. Atmos. Sci.*, **31**, 581–592, doi:10.1007/s00376-013-3115-y.

Pardo-Rodriguez, L., 2009: Lightning activity in Atlantic tropical cyclones: Using the Long-Range Lightning Detection Network (LLDN). UCAR Libraries, 12 pp. [Available online at http://opensky.library.ucar.edu/collections/SOARS-000-000-000-193.]

Petersen, W. A., S. A. Rutledge, and R. E. Orville, 1996: Cloud-to-ground lightning observations from TOGA COARE: Selected results and lightning location algorithms. *Mon. Wea. Rev.*, **124**, 602–620, doi:10.1175/1520-0493(1996)124<0602:CTGLOF>2.0.CO;2.

——, R. C. Cifelli, S. A. Rutledge, B. S. Ferrier, and B. F. Smull, 1999: Shipborne dual-Doppler operations and observations during TOGA COARE. *Bull. Amer. Meteor. Soc.*, **80**, 81–97, doi:10.1175/1520-0477(1999)080<0081:SDDODT>2.0.CO;2.

——, H. J. Christian, and S. A. Rutledge, 2005: TRMM observations of the global relationship between ice water content and lightning. *Geophys. Res. Lett.*, **32**, L14819, doi:10.1029/2005GL023236.

Powell, M. D., S. H. Houston, L. R. Amat, and N. Morisseau-Leroy, 1998: The HRD real-time hurricane wind analysis system. *J. Wind Eng. Ind. Aerodyn.*, **77–78**, 53–64.

Price, C., M. Asfur, and Y. Yair, 2009: Maximum hurricane intensity preceded by increase in lightning frequency. *Nat. Geosci.*, **2**, 329–332, doi:10.1038/ngeo477.

Rawlins, F., 1982: A numerical study of thunderstorm electrification using a three dimensional model incorporating the ice phase. *Quart. J. Roy. Meteor. Soc.*, **108**, 779–800, doi:10.1002/qj.49710845804.

Reinhart, B., and Coauthors, 2014: Understanding the relationships between lightning, cloud microphysics, and airborne radar-derived storm structure during Hurricane Karl (2010). *Mon. Wea. Rev.*, **142**, 590–605, doi:10.1175/MWR-D-13-00008.1.

Reisner, J. M., A. Mousseau, A. A. Wyszogrodzki, and D. A. Knoll, 2005: An implicitly balanced hurricane model with physics-based preconditioning. *Mon. Wea. Rev.*, **133**, 1003–1022, doi:10.1175/MWR2901.1.

Rogers, R. F., M. L. Black, S. S. Chen, and R. A. Black, 2007: An evaluation of microphysics fields from mesoscale model simulations of tropical cyclones. Part I: Comparisons with observations. *J. Atmos. Sci.*, **64**, 1811–1834, doi:10.1175/JAS3932.1.

Rogers, R. R., and M. K. Yau, 1989: *A Short Course in Cloud Physics*. 3rd ed. Pergamon Press, 293 pp.

Rotunno, R., Y. Chen, W. Wang, C. Davis, J. DuDhia, and G. J. Holland, 2009: Large-eddy simulation of an idealized tropical cyclone. *Bull. Amer. Meteor. Soc.*, **90**, 1783–1788, doi:10.1175/2009BAMS2884.1.

Samsury, C. E., and R. E. Orville, 1994: Cloud-to-ground lightning in tropical cyclones: A study of Hurricanes Hugo (1989) and Jerry (1989). *Mon. Wea. Rev.*, **122**, 1887–1896, doi:10.1175/1520-0493(1994)122<1887:CTGLIT>2.0.CO;2.

Saunders, C. P. R., and L. S. Peck, 1998: Laboratory studies of the influence of the rime accretion rate on charge transfer during crystal/graupel collisions. *J. Geophys. Res.*, **103**, 13 949–13 956, doi:10.1029/97JD02644.

——, W. D. Keith, and R. P. Mitzeva, 1991: The effect of liquid water on thunderstorm charging. *J. Geophys. Res.*, **96**, 11 007–11 017, doi:10.1029/91JD00970.

——, L. S. Peck, G. G. Aguirre Varela, E. E. Avila, and N. E. Castellano, 2001: A laboratory study of the influence of water vapour on the charge transfer during collisions between ice crystal and graupel. *J. Atmos. Res*, **58**, 187–203, doi:10.1016/S0169-8095(01)00090-4.

Schultz, C. J., W. A. Petersen, and L. D. Carey, 2011: Lightning and weather: A comparison between total and cloud-to-ground lightning trends. *Wea. Forecasting*, **26**, 744–755, doi:10.1175/WAF-D-10-05026.1.

Shao, X.-M., and Coauthors, 2005: Katrina and Rita were lit up with lightning. *Eos, Trans. Amer. Geophys. Union*, **86**, 398, doi:10.1029/2005EO420004.

——, M. Stanley, A. Regan, J. Harlin, M. Pongratz, and M. Stock, 2006: Total lightning observations with the new and improved Los Alamos Sferic Array (LASA). *J. Atmos. Oceanic Technol.*, **23**, 1273–1288, doi:10.1175/JTECH1908.1.

Shapiro, L. J., 1983: The asymmetric boundary layer flow under a translating hurricane. *J. Atmos. Sci.*, **40**, 1984–1998, doi:10.1175/1520-0469(1983)040<1984:TABLFU>2.0.CO;2.

——, and J. L. Franklin, 1999: Potential vorticity asymmetries and tropical cyclone motion. *Mon. Wea. Rev.*, **127**, 124–131, doi:10.1175/1520-0493(1999)127<0124:PVAATC>2.0.CO;2.

Skamarock, W. C., and J. B. Klemp, 2008: A time-split nonhydrostatic atmospheric model for research and NWP applications. *J. Comput. Phys.*, **227**, 3465–3485, doi:10.1016/j.jcp.2007.01.037.

Squires, K., and S. Businger, 2008: The morphology of eyewall lightning outbreaks in two category 5 hurricanes. *Mon. Wea. Rev.*, **136**, 1706–1726, doi:10.1175/2007MWR2150.1.

Stern, D. P., and D. S. Nolan, 2009: Reexamining the vertical structure of tangential winds in tropical cyclones: Observations and theory. *J. Atmos. Sci.*, **66**, 3579–3600, doi:10.1175/2009JAS2916.1.

Stevenson, S. N., K. L. Corbosiero, and J. Molinari, 2014: The convective evolution and rapid intensification of Hurricane Earl (2010). *Mon. Wea. Rev.*, **142**, 4364–4380, doi:10.1175/MWR-D-14-00078.1.

Straka, J. M., and E. R. Mansell, 2005: A bulk microphysics parameterization with multiple ice precipitating categories. *J. Appl. Meteor.*, **44**, 445–466, doi:10.1175/JAM2211.1.

Takahashi, T., 1978: Riming electrification as a charge generation mechanism in thunderstorms. *J. Atmos. Sci.*, **35**, 1536–1548, doi:10.1175/1520-0469(1978)035<1536:REAACG>2.0.CO;2.

Thomas, J. N., N. N. Solorzano, S. A. Cummer, and R. H. Holzworth, 2010: Polarity and energetics of inner core lightning in three intense North Atlantic hurricanes. *J. Geophys. Res.*, **115**, A00E15, doi:10.1029/2009JA014777.

Weiss, S. A., D. R. MacGorman, and K. M. Calhoun, 2012: Lightning in the anvils of supercell thunderstorms. *Mon. Wea. Rev.*, **140**, 2064–2079, doi:10.1175/MWR-D-11-00312.1.

Wiens, K. C., S. A. Rutledge, and S. A. Tessendorf, 2005: The 29 June 2000 supercell observed during STEPS. Part II: Lightning and charge structure. *J. Atmos. Sci.*, **62**, 4151–4177, doi:10.1175/JAS3615.1.

Williams, E. R., 1989: The tripole structure of thunderstorms. *J. Geophys. Res.*, **94**, 13 151–13 167, doi:10.1029/JD094iD11p13151.

——, and S. Stanfill, 2002: The physical origin of the land–ocean contrast in lightning activity. *C. R. Phys.*, **3**, 1277–1292, doi:10.1016/S1631-0705(02)01407-X.

——, C. M. Cooke, and K. A. Wright, 1985: Electrical discharge propagation in and around space charge cloud. *J. Geophys. Res.*, **90**, 6059–6070, doi:10.1029/JD090iD04p06059.

Zhang, F., and J. A. Sippel, 2009: Effects of moist convection on hurricane predictability. *J. Atmos. Sci.*, **66**, 1944–1961, doi:10.1175/2009JAS2824.1.

Zhang, J., and Coauthors, 2011: National Mosaic and Multi-Sensor QPE (NMQ) system: Description, results, and future plans. *Bull. Amer. Meteor. Soc.*, **92**, 1321–1338, doi:10.1175/2011BAMS-D-11-00047.1.

Ziegler, C. L., and D. R. MacGorman, 1994: Observed lightning morphology relative to modeled space charge and electric field distributions in a tornadic storm. *J. Atmos. Sci.*, **51**, 833–851, doi:10.1175/1520-0469(1994)051<0833:OLMRTM>2.0.CO;2.

——, ——, J. E. Dye, and P. S. Ray, 1991: A model evaluation of noninductive graupel-ice charging in the early electrification of a mountain thunderstorm. *J. Geophys. Res.*, **96**, 12 833–12 855, doi:10.1029/91JD01246.